



**HAL**  
open science

# CIPFAR: A 3D unified numerical framework for the modeling of ductile fracture based on the phase field model and adaptive remeshing

Hazem Eldahshan, José Alves, Pierre-Olivier Bouchard, Etienne Perchat,  
Daniel Pino Munoz

► **To cite this version:**

Hazem Eldahshan, José Alves, Pierre-Olivier Bouchard, Etienne Perchat, Daniel Pino Munoz. CIPFAR: A 3D unified numerical framework for the modeling of ductile fracture based on the phase field model and adaptive remeshing. *Computer Methods in Applied Mechanics and Engineering*, 2021, 387, pp.114171. 10.1016/j.cma.2021.114171 . hal-03472614

**HAL Id: hal-03472614**

**<https://minesparis-psl.hal.science/hal-03472614>**

Submitted on 17 Mar 2022

**HAL** is a multi-disciplinary open access archive for the deposit and dissemination of scientific research documents, whether they are published or not. The documents may come from teaching and research institutions in France or abroad, or from public or private research centers.

L'archive ouverte pluridisciplinaire **HAL**, est destinée au dépôt et à la diffusion de documents scientifiques de niveau recherche, publiés ou non, émanant des établissements d'enseignement et de recherche français ou étrangers, des laboratoires publics ou privés.



Distributed under a Creative Commons Attribution - NonCommercial 4.0 International License

# CIPFAR: A 3D unified numerical framework for the modeling of ductile fracture based on the phase field model and adaptive remeshing

Hazem Eldahshan<sup>a,b</sup>, José Alves<sup>b</sup>, Pierre-Olivier Bouchard<sup>a</sup>, Etienne Perchat<sup>b</sup>, Daniel Pino Munoz<sup>a</sup>

<sup>a</sup>*MINES Paris-Tech, PSL- Research University, CEMEF – Center for Material Forming, CNRS UMR 7635, BP 207, 1 rue Claude Daunesse, 06904 Sophia Antipolis Cedex, France*

<sup>b</sup>*Transvalor SA, E-Golf Park, 950 Avenue Roumanille, 06410 Biot, France*

---

## Abstract

In this paper, a general numerical framework for the modeling of ductile fracture in 3D meshes is introduced. The strategy is inspired from the phase field model and adaptive remeshing tools. The phase field model was introduced as a continuous model for predicting the initiation and propagation of cracks in materials. However, the model has a limitation on the choice of the characteristic length scale that controls the width of the cracked region. This work contributes to the full modeling of transition between the continuous damage using the phase field model to the discontinuous crack initiation and propagation within a unified numerical framework called CIPFAR. The contributions of the work include: (i). identification of the crack surface on arbitrary mesh topologies; (ii). intersection by a Sequence Agnostic Partitioning strategy which is introduced to adapt the mesh to the computed crack surface; (iii). a nodal duplication by virtual non-manifold patch repair to open the mesh. Combining all the mentioned algorithms with adaptive remeshing allows modeling the initiation and propagation of cracks in materials efficiently. Different numerical examples are presented to prove the ability of the developed algorithm to model ductile fracture cases without the need to predefine the crack initiation region.

*Keywords:* Phase field model, Adaptive remeshing, Ductile fracture, Crack insertion and propagation

---

## 1. Introduction

The modeling of initiation and propagation of cracks in continuum media has been considered as one of the most important and challenging research areas in mechanical engineering in the last decades. There is almost no engineering applications that is not concerned with the study of crack formation such as: aerospace, automotive and energy sectors. Fracture mechanisms and propagation prediction process could be very complex and hence a suitable computational tool is needed to model the process with high precision and low computational cost.

Modeling techniques in fracture mechanics can be divided in two categories: (i). brittle fracture; (ii). ductile fracture. In brittle fracture, the plasticity is confined to a region that is small compared to the crack length. The fracturing process is mainly based on the creation of new crack surfaces. One of the first attempts to predict the onset of failure in brittle materials was a theory based on Griffith's hypothesis [1] in which a competition between internal elastic and fracture energies leads

to the onset of fracture, i.e., the creation of new crack surfaces. The theory of Griffith is able to predict the critical moment for pre-cracked bodies at which the crack propagation is triggered. The main drawback of the Griffith criterion is that it deals with pre-cracked bodies where the crack tip is predefined and predicts the critical failure load with no description on the initiation and propagation mechanisms. Later on, Irwin defined the stress intensity factors in order to describe the stress state around the crack tip in a finite medium [2].

Francfort and Marigo proposed in [3] a mathematical generalization of the Griffith theory in which a minimization of an energy functional that contains the elastic and fracture energies enables the prediction of initiation, propagation, merging and branching of crack branches in brittle materials. A regularized formulation of the problem was proposed by Ambrosio and Tortorelli [4] in which the sharp crack is replaced by a continuous field known as the "Phase field" that goes from 0 (intact material) to 1 (totally damaged) with a length scale that controls its sharpness. Within the framework of finite elements, the smallest mesh size needs to be small enough for an accurate resolution of the field. An uncoupled computational strategy known as "Staggered algorithm" is used to solve the system of equations to fully describe the cracking process. Later on, many extensions to the ductile fracture have been proposed in the literature. The main aim was to introduce the effect of plastic strain in the crack driving force. M. Ambati et al. [5, 6] coupled the equivalent plastic strain with the elastic degradation function through an exponential form. Borden et al. [7] also added an effective plastic energy component degraded by a plastic degradation function.

Modeling techniques in ductile fracture can be divided in two categories: i. continuous models, ii. discrete models. In continuous models, an isotropic/anisotropic damage field is defined within the context of continuum mechanics and associated to the bulk material in which its evolution at the macro scale describes the nucleation, growth and coalescence of voids at the micro scale [8]. The damage field degrades the material properties as a response to the evolution of the micro voids. A main drawback of such description is the inability to model the discontinuous transition to fracture where a discrete crack surface is introduced in the medium at the macro-scale. This results in an accumulation of a highly strained material in the low stress cracked region as previously shown in [9]. Among the former, we can count the damage models that are based on either micro-mechanical or phenomenological descriptions. In the initial model of Gurson [10], the level of porosity in the material is coupled with the yield surface through a void fraction function in order to model the effect of damage on the mechanical behaviour. An improved GTN model [11] uses more parameters to give a better description of the growth of voids. The phenomenological models are semi empirical models that uses some mechanical fields such as the plastic deformation and stress state to describe the level of damage in the material. The Lemaitre model [12] is a thermodynamically consistent damage model that is mainly based on the stress triaxiality. An enhanced Lemaitre model [13] was also introduced to include the effect of plastic deformations and limit the evolution of damage beyond a given threshold of the stress triaxiality. Another enhancement to the model was presented by T.-S. Cao et al. in [14] by including the effect of the Lode parameter.

Contrary to continuous models, discrete models provide an accurate description of the transition from damage to fracture by modeling the decohesion of the crack faces. One of the initial attempts to model the discrete crack propagation with remeshing within the context of ductile fracture was proposed in 2D by J. Mediavilla et al. [9] in combination with a continuum damage model. The crack propagation direction is the one that leads to the maximum damage in the material at different distances from the crack tip. The results were very promising, however this approach

might lead to wrong crack directions especially in the case of complex crack patterns, merging, branching and multiple cracks. In addition, the extension to 3D is not straight forward. S. Feld-Payet et al. [15] introduced a marching ridges algorithm that uses a damage function in order to identify the crack surface intersection in regularized media. The idea is very similar to finding a corner or edge in an image as explained in [16] in which authors proposed a marching lines algorithm able to extract the crest lines in an image. In 2D, an initial point that lies on the crack surface is chosen as the point that has the maximum damage. An evaluation circle with some radius was then used to find another local maximum. In 3D, the same idea as in 2D is used to construct the crack front by performing a search in three orthogonal planes, then the crack segment is constructed by performing another search in the planes orthogonal to each segment.

The extended finite element method XFEM was introduced in [17] as a numerical technique that handles the existence of cracks in brittle fracture by incorporating discontinuous functions to the classical finite element method. The main advantage is that the crack can be propagated within the mesh without any remeshing. However, the need of remeshing in ductile fracture is essential especially in large deformations which makes the use of XFEM very limited due to the complexity of the transfer of fields after remeshing and applying the incompressibility constraints [18].

Another discrete modeling technique is the use of remeshing in order to introduce the discontinuity in the medium. P.O. Bouchard et al. introduced in [19] a numerical framework for the modeling of crack propagation in 2D with a comparison between different propagation criteria. Ali Hussein et al. [20] presented a strategy that uses the phase field solution in order to detect the crack path. Then, a specific cutting algorithm is developed using the virtual elements method [21, 22] in order to open the crack lips once the nodes that lie on the crack surface are duplicated. Another use of remeshing was introduced in [23] within the context of cohesive element modeling. The algorithm begins by detecting the crack propagation angle, then a remeshing operation is carried out to insert nodes on the detected crack path followed by insertion of cohesive elements.

The main objective of this work is to provide a unified 3D model CIPFAR (Crack Insertion and propagation using the Phase Field and Adaptive Remeshing) for predicting initiation, propagation, merging and branching of cracks in an elasto-plastic medium by combining the phase field model with adaptive remeshing tools. The main features of the presented algorithm are: (i). the simplicity and robustness regardless of the constitutive law; (ii). designed for the purpose of parallel computations; (iii). can handle complex cracking patterns without any additional ad-hoc criteria. The article is organized as follows: Section 2 introduces the phase field model formulation used in this work. In section 3, the crack insertion algorithm is described in details with three numerical examples dedicated to ductile fracture presented in section 4. Finally, a conclusion with some perspectives for the future work is given in section 5.

## 2. The phase field model for ductile fracture

In this section, the governing equations of the phase field model along with the mechanical formulation of the problem is presented.

### 2.1. General formulation of the phase field model

A Mumford–Shah [24] type free energy functional  $\mathcal{E}$  was introduced by Francfort and Marigo in [3] as a generalization of Griffith criterion for fracture [1] in brittle materials. The minimization of

the proposed functional with respect to its two parameters  $\mathbf{u}$  and  $\Gamma$  leads to an energetic description of the fracturing process including the initiation, propagation, merging and branching of cracks.

$$\mathcal{E}(\mathbf{u}, \Gamma) = \int_{\Omega} W_e(\boldsymbol{\varepsilon}^e) d\Omega + \int_{\Gamma} G_c d\partial\Omega \quad (1)$$

$W_e$  is the elastic strain energy,  $G_c$  is the fracture toughness,  $\mathbf{u}$  is the displacement vector,  $\Gamma$  is the discrete crack surface and  $\Omega$  is the volume of the domain as shown in Fig. 2a.

The treatment of the introduced energy functional is not suitable for numerical implementation since the second integral is carried out over an unknown crack surface. A regularized functional  $\mathcal{E}_l$  was introduced by Ambrosio and Tortorelli in [4] that transforms the discrete crack topology by a scalar field parameter  $d$  that varies between 0 (solid material) and 1 (fully damaged material) as shown in Fig. 2b with a characteristic length scale  $l_c$  that manages the width of the damaged zone

$$\mathcal{E}_l(\mathbf{u}, d) = \int_{\Omega} g_e(d) W_e(\boldsymbol{\varepsilon}^e) d\Omega + \int_{\Omega} \frac{G_c}{2l_c} (d^2 + l_c^2 |\nabla d|^2) d\Omega \quad (2)$$

with an elastic degradation function that couples the effect of crack propagation on the bulk material

$$g_e(d) = (1 - d)^2 + \zeta \quad (3)$$

where  $\zeta$  is a numerical parameter usually chosen as  $10^{-6}$  in order to prevent numerical singularities. The minimization of the regularized energy functional with respect to the phase field variable leads to the following equations

$$\begin{cases} \frac{G_c}{l_c} (d - l_c^2 \nabla^2 d) = -g'_e(d) \mathcal{H}(\underline{\mathbf{x}}, t) & \text{(Evolution of the phase field)} & (4a) \\ \mathcal{H} = \max_n W_e(\boldsymbol{\varepsilon}^e(\underline{\mathbf{x}}, d_n)) & \text{(Local history functional)} & (4b) \\ \nabla d \cdot \mathbf{n} = 0 & \text{(Neumann boundary condition)} & (4c) \end{cases}$$

The homogeneous solution of the phase field differential equation in 1D can be proven to be as follows[25]

$$d(x) = \exp\left(\frac{-|x|}{l_c}\right) \quad (5)$$

The phase field solution and its derivative are illustrated in Fig. 1. It is clear that the phase field function is non differentiable at  $x = 0$ , i.e., the gradient is undefined. In order to describe the initiation and propagation of cracks in ductile materials, Borden et al. [7] modified the local history functional that appears in equation 4b as follows

$$\mathcal{H} = \beta_1 g'_e(d) \max_n W_e(\boldsymbol{\varepsilon}^e(\underline{\mathbf{x}}, d_n)) + \beta_2 g'_p(d) \langle W_p(\bar{\boldsymbol{\varepsilon}}) - W_0 \rangle \quad (6)$$

the angle bracket operator is defined as follows:

$$\langle x \rangle = \begin{cases} x & x \geq 0 \\ 0 & x < 0 \end{cases}$$

where  $W_p$  is the plastic energy density,  $g_p$  is a plastic degradation function that is chosen as the same as the elastic degradation function,  $W_0$  is a plastic energy threshold,  $\beta_1$  and  $\beta_2$  are numerical parameters used to calibrate the model with the experiments.

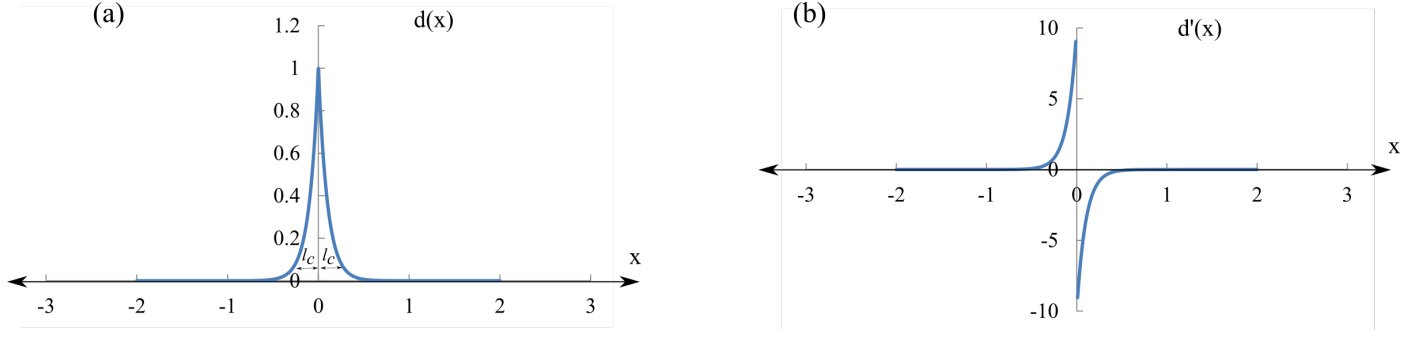


**Figure 1:** Phase field approximation in 1D along with its derivative.

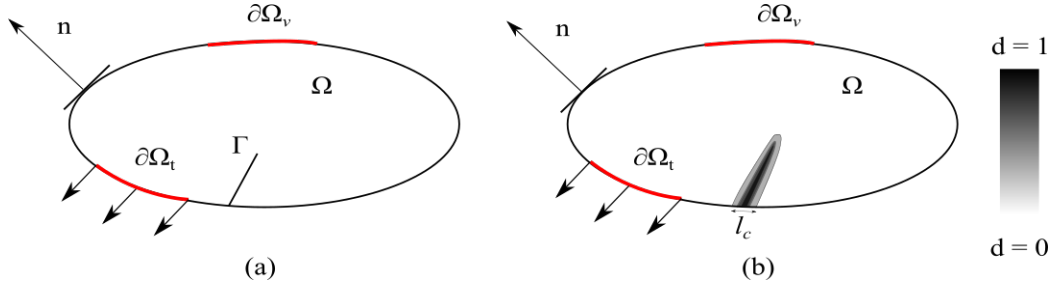


**Figure 2:** Geometry and boundary conditions of a domain with discontinuity  $\Gamma$  in (a). Phase field regularization of the crack topology in (b).

A mixed velocity/pressure finite element model is used for the mechanical computations. In order to prevent the volumetric locking associated with the incompressible behaviour of the plastic deformation, a P1+/P1 stabilization has been used. The final formulation satisfies the Brezzi-Babuska inf-sup condition [26, 27]. The mesh is built using tetrahedral elements. The strong and weak formulation of the mechanical and phase field equations can be found in appendix A.

## 2.2. Elasto-plastic model

Starting with the assumption of linear isotropic elasticity, the equivalent plastic strain increment is calculated using the return mapping algorithm at the increment  $n + 1$  as follows

$$\mathbf{s}^{trial} = 2\mu g_e(d_n) [\boldsymbol{\varepsilon}_{n+1} - \boldsymbol{\varepsilon}_n^p] \quad (7a)$$

$$f^{trial} = \sqrt{3 J_2(\mathbf{s}_{n+1}^{trial})} - g_p(d_n) \boldsymbol{\sigma}_y(\bar{\boldsymbol{\varepsilon}}_n) \leq 0 \quad (7b)$$

with  $\mu$  defined in terms of Young's modulus  $E$  and Poisson's ratio  $\nu$  as follows

$$\mu = \frac{E}{2(1 + \nu)}$$

where  $\mathbf{s}^{trial}$  is the trial deviatoric stress,  $\boldsymbol{\varepsilon}$  is the total strain tensor,  $\boldsymbol{\varepsilon}^p$  is the plastic strain tensor,  $\bar{\boldsymbol{\varepsilon}}$  is the equivalent plastic strain,  $J_2$  is the second invariant of the deviatoric stress tensor,  $g_p$  is the plastic degradation function that is chosen to be the same as the elastic degradation function  $g_e$  and  $n$  is the increment number. If the condition in 7b is not satisfied, a new plastic deformation increment is found as follows

$$f = \sqrt{3 J_2(\mathbf{s}_{n+1}^{trial})} - g_p(d_n) \boldsymbol{\sigma}_y(\bar{\boldsymbol{\varepsilon}}_{n+1}) - 3\mu g_p(d_n) \Delta\lambda = 0 \quad (8)$$

In this study, the effective stress  $\boldsymbol{\sigma}_y$  is defined according to two material hardening laws as follows

$$\boldsymbol{\sigma}_y = \sigma_0 + H\bar{\boldsymbol{\epsilon}}, \quad (\text{Linear hardening}) \quad (9a)$$

$$\boldsymbol{\sigma}_y = \sigma_\infty + (\sigma_0 - \sigma_\infty)e^{(-\delta\bar{\boldsymbol{\epsilon}})}, \quad (\text{Nonlinear hardening}) \quad (9b)$$

where  $\sigma_0$  is the initial yield stress and  $H$  is the plastic modulus,  $\sigma_\infty$  is the ultimate strength and  $\delta$  is the saturation coefficient. It should be noted that  $d_n$  is constant in equation 8 where no kinematic hardening is considered. A Newton-Raphson nonlinear solver is used to solve equation 8, the equivalent plastic strain update is written as

$$\bar{\boldsymbol{\epsilon}}_{n+1} = \bar{\boldsymbol{\epsilon}}_n + \Delta\lambda \quad (10)$$

where  $\lambda$  is the plastic multiplier. The update of the deviatoric stress tensor and discrete tangent modulus are expressed as follows

$$\mathbf{s}_{n+1} = \frac{\mathbf{s}_{n+1}^{trial}}{1 + \frac{3\mu g(d_n)\Delta\lambda}{\sigma_0(\bar{\boldsymbol{\epsilon}}_{n+1})}} \quad (11)$$

$$C_{n+1}^d = \frac{\partial \dot{\mathbf{s}}^{n+1}}{\partial \dot{\boldsymbol{\epsilon}}^{n+1}} = 2\mu g(d_n) \left( 1 - 6 \frac{\mu^2 \Delta\lambda}{J_2(\mathbf{s}_{n+1}^{trial})} \mathbf{I}^{dev} \right) - 4\mu^2 \bar{\mathbf{n}} \otimes \bar{\mathbf{n}} \left( \frac{1}{\frac{\partial \sigma_y}{\partial \delta \lambda} + 3\mu g(d_n)} + \frac{\Delta\lambda}{J_2(\mathbf{s}_{n+1}^{trial})} \right) \quad (12)$$

where  $\bar{\mathbf{n}} = \frac{3}{2} \frac{\mathbf{s}}{J_2(\mathbf{s}_{n+1})}$  and  $\otimes$  is the outer product.

### 2.3. Adaptive remeshing strategy

An adaptive remeshing strategy developed in [28] is used in this algorithm. The main objective is to refine the mesh automatically in the locations where the crack is expected to propagate. Two main thresholds are introduced in order to achieve this purpose as follows:

- A remeshing indicator function: this is a metric that indicates when and where the mesh should be refined. This function needs to properly describe the evolution of the crack [28].
- A volume quality control: this function is introduced in order to control the number of remeshing operations and hence minimize the numerical loss associated with the transfer of fields during remeshing.

The remeshing indicator function could be chosen as one of the following functions: (i). the phase field function; (ii). the equivalent plastic strain; (iii). the normalized yielding function. In this article, the equivalent plastic strain is used for all the numerical examples. The adaptive mesh refinement helps in accurately resolving the phase field equation and also to reduce the computation time throughout the simulation.

## 3. Crack insertion algorithm

In this section, a numerical strategy for the simulation of discrete crack insertion and propagation is presented within the context of Finite element analysis. The phase field solution provides a highly concentrated damage field in which the crack surface can be identified as the points that

have a phase field value of 1. However, due to the numerical approximation, the continuity condition of the phase field gradient <sup>1</sup> leads to a diffused zone of the crack, i.e., there is a finite zone that has a phase field value very close to 1 as can be seen in Fig. 3. In this work, we propose a strategy that is based on the phase field gradient in order to identify the crack surface by combining the phase field solution along with its gradient. The idea of our algorithm is to simplify the crack surface identification methodology for three main reasons: (i). the search process must be independent on the choice of model parameters such as the radius of the evaluation circle as presented in [15]; (ii). the algorithm should be independent on the starting point, in other words, an agnostic search of identifying the crack surfaces; (iii). to have an algorithm that can be used for parallel computations by construction.

The other crucial point in the algorithm is the insertion of the discrete crack topology in the mesh. A numerical strategy is designed for this purpose where it can be divided in four main steps: (i). an identification of the intersection between the crack surface and the finite element mesh; (ii). a local modification of the mesh topology by partitioning the elements being intersected by the crack surface; (iii). a new strategy based on the well known coloring algorithm in the graph theory [29] is presented in order to duplicate the nodes that lie on the crack surface; (iv). a volumetric remeshing operation is carried out in order to ensure a good quality of elements throughout the computations. It is worth mentioning that there are other approaches in the literature that are designed for similar purposes. For example, M. Shakoor et al. introduced in [30] a body-fitted method for the modeling of ductile fracture simulations. In this work, a level set function is used to define the void/matrix interface where the mesh is adapted accordingly.

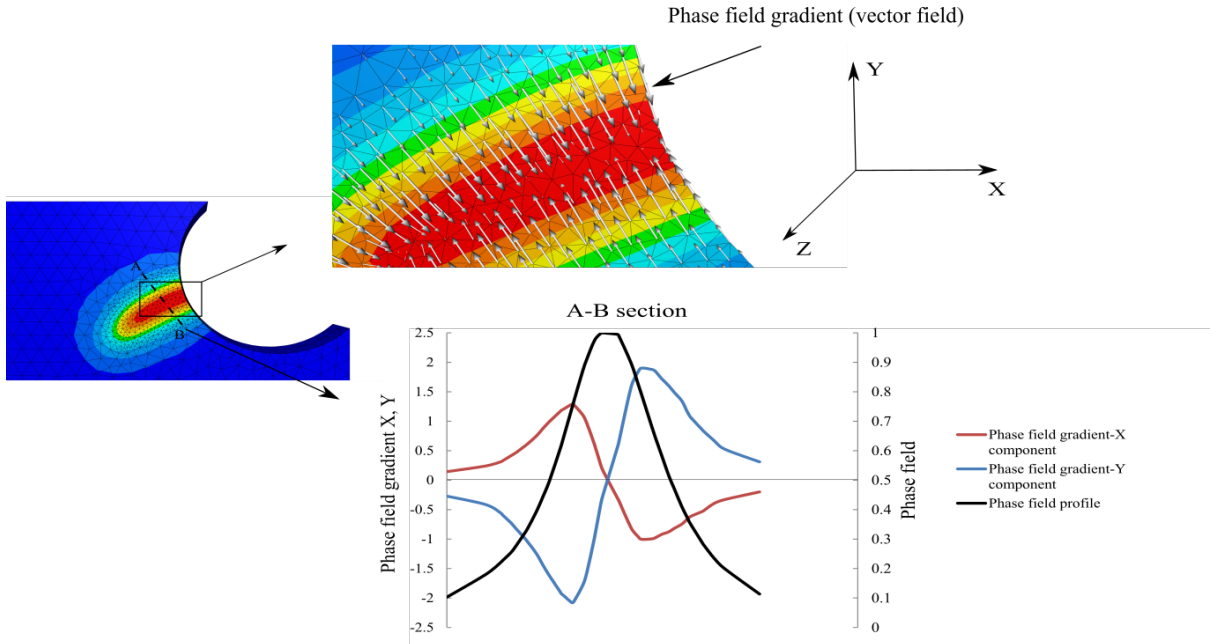


**Figure 3:** Phase field computation on a finite element mesh. The vector field of the phase field gradient is shown (top). The phase field along with the gradient components profiles projected on the X-Y plane are computed (bottom).

<sup>1</sup>The continuity of the phase field solution and its gradient within the elements are imposed in the weak formulation of the problem (See appendix A for more details). However, the solution of the homogeneous differential equation of the phase field as shown in Fig. 1 shows that the gradient is undefined at the crack interface.

### 3.1. Identification of crack surface intersection locations

Starting with the continuous phase field  $d$ , a point is identified to lie on the crack surface if it satisfies the following two conditions:

$$\begin{cases} \mathbf{V}^t \nabla d = 0 & (13a) \\ \mathbf{V}^t Hess(d) \mathbf{V} = 0 & (13b) \end{cases}$$

where  $\mathbf{V}$  is a  $n \times k$  matrix in which  $n$  is the dimension of the space and  $k$  is the number of linearly independent vectors that span the search space. The second condition is automatically satisfied since the search process is limited in the region where the phase field is very close to 1 which is convex by definition. In consequence, the satisfaction of condition 13a necessitates at least the  $C^1$  continuity of the phase field solution. This critical point represents a  $(n-1)$ -dimensional height ridge in a  $n$ -dimensional space according to the definition of D. Eberly et al. in [31]. In other words, the search space is restricted to a subspace spanned by a vector.

The crack surface identification algorithm can be explained in three main steps: (i). smoothing the phase field gradient on all the mesh nodes; (ii). calculating the projection of the phase field gradient along the vector connecting the two nodes (along the edge direction); (iii). identifying the location on the edge that vanishes that gradient projection which represents a height ridge. The selection of an edge to be tested should satisfy a condition of having a value of phase field greater than a given threshold very close to 1 (normally the threshold is chosen to be 0.99) for at least one of its two nodes as shown in Fig. 4. The search direction is chosen to be the unit vector that is aligned along an edge in the mesh. The projection of the phase field gradient is calculated as follows:

$$\nabla d_{i,j}^{proj} = \nabla d_{i,j}^{nodal} \cdot \vec{r} \quad (14)$$

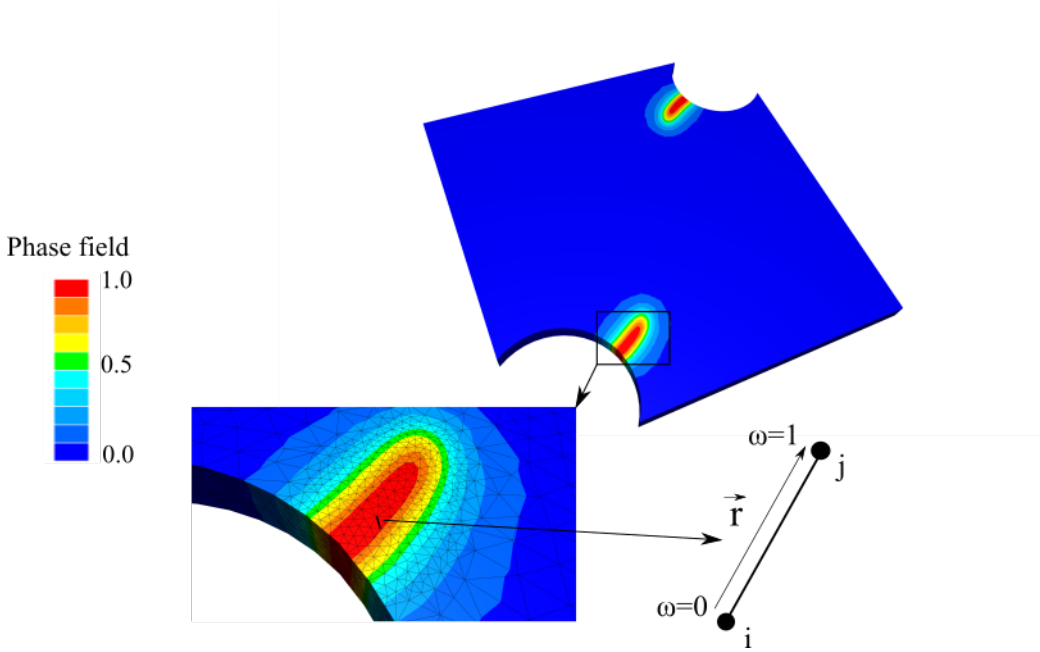


**Figure 4:** Selection of the candidate edges for the crack intersection.

where  $i$  and  $j$  are the node index,  $\nabla d_{i,j}^{nodal}$  is the phase field gradient calculated at the nodes  $i, j$ ,  $\nabla d_{i,j}^{proj}$  is the projection of the phase field gradient calculated at nodes  $i, j$  and  $\vec{r}$  is the position unit

vector as shown in Fig. 4. A linear interpolation in terms of the non-dimensional parameter  $\omega$  is given as:

$$\nabla d_i^{proj} + \omega_c (\nabla d_j^{proj} - \nabla d_i^{proj}) = 0 \quad (15)$$

where  $\omega_c$  is a non-dimensional distance of the critical point calculated along the edge length. Solving equation 15 for  $\omega_c$  with the condition that  $0 < \omega_c < 1$  gives the intersection of the crack surface with the edge. Another condition is added to ensure that the material point at the selected  $\omega_c$  has reached a maximum level of degradation as follows:

$$d_i^{nodal} + \omega_c (d_j^{nodal} - d_i^{nodal}) \geq 0.99 \quad (16)$$

Fig. 10a shows the identified locations of the intersection between the crack surface and the mesh calculated using the presented strategy.

In the next section, the smoothing operation that transforms the phase field gradient from a P0 (constant per element) to a P1 (nodal) field is presented.

### 3.2. Phase field gradient smoothness

In this section, a smoothing operation of the phase field gradient from a P0 field which is constant per element to a nodal P1 field is achieved. The gradient calculation represents an important part in the crack insertion algorithm as it is the essential component in the identification of the crack surface intersection with the mesh. The aim is to reduce the numerical error during the smoothing of fields in order to have a good resolution of the phase field gradient. Different smoothing methods can be found in the literature [32, 33]. Two methods are used in this work: (i). average smoothing method; (ii). Galerkin's smoothing method.

#### 3.2.1. Average smoothing method

This is the simplest method of a P0 field smoothing. The nodal phase field gradient  $\nabla d_i^{nodal}$  is calculated as

$$\nabla d_i^{nodal} = \frac{\sum_{i=1}^{N_{ep}} \nabla d_i^{elem}}{N_{ep}} \quad (17)$$

where  $d_i^{elem}$  is the phase field gradient calculated per element and  $N_{ep}$  is the total number of elements in the patch of elements containing the node.

#### 3.2.2. Galerkin's smoothing method

The weak form of the transformation of the phase field gradient from a P0 field to a P1 field (nodal) applied over an element gives

$$\int_{\Omega} \vec{\phi}_h \nabla d^{nodal} d\Omega = \int_{\Omega} \vec{\phi}_h \nabla d^{elem} d\Omega \quad (18)$$

The functions  $\nabla d^{nodal}$  and  $\vec{\phi}_h$  are defined as follows

$$\vec{\phi}_h(\vec{x}) = \sum_{k=1}^{N_n} N_k(\vec{x}) c_k \quad (19a)$$

$$\nabla d^{nodal}(\vec{x}) = \sum_{k=1}^{N_n} N_k(\vec{x}) d_k \quad (19b)$$

where  $\vec{\phi}_h$  are the test functions,  $c_k$  and  $d_k$  are the degrees of freedom of the test and trial solutions, respectively.  $N_k$  are the same basis functions used in the finite element model and  $N_n$  is the number of basis functions.

### 3.2.3. Controlling the crack increment length

According to the Griffith criterion of fracture, an infinitesimal crack area increment  $dA$  can be calculated as follows [1]

$$dA = l_f da = \frac{d\psi_{frac}}{G_c} \quad (20)$$

where  $l_f$  is the length of the crack front and  $da$  is the crack increment length as shown in Fig. 5,  $\psi_{frac}$  is the fracture energy which is defined in the regularized form as follows:

$$\psi_{frac}^{reg} = \int_{\Omega} \frac{G_c}{2l_c} (d^2 + l_c^2 |\nabla d|^2) d\Omega \quad (21)$$

The effective crack area increment can be then calculated as

$$\Delta A^{eff} = \frac{\psi_{n+1}^{reg} - \psi_n^{reg}}{G_c} \quad (22)$$

Where the total effective crack area at increment  $n + 1$  can be calculated as

$$A_{n+1}^{eff} = A_n^{eff} + \Delta A^{eff} \quad (23)$$

The condition at which a crack increment is inserted is defined as follows:

$$A_{n+1}^{eff} \geq A_{fixed} \quad (24)$$

where  $A_{fixed}$  is a predefined parameter used to control the moment at which a crack increment is inserted. The effect of the crack increment length on the crack propagation is studied in the numerical examples in section 4.

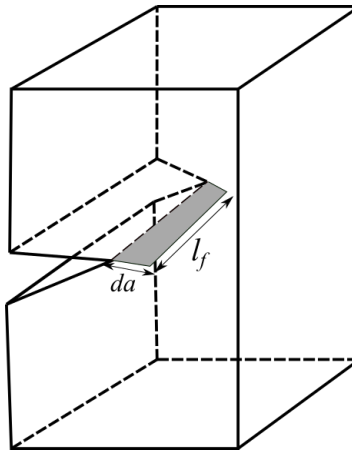


**Figure 5:** Illustration of the surface topology of a crack increment.

### 3.3. Fracture surface intersection by Sequence Agnostic Partitioning

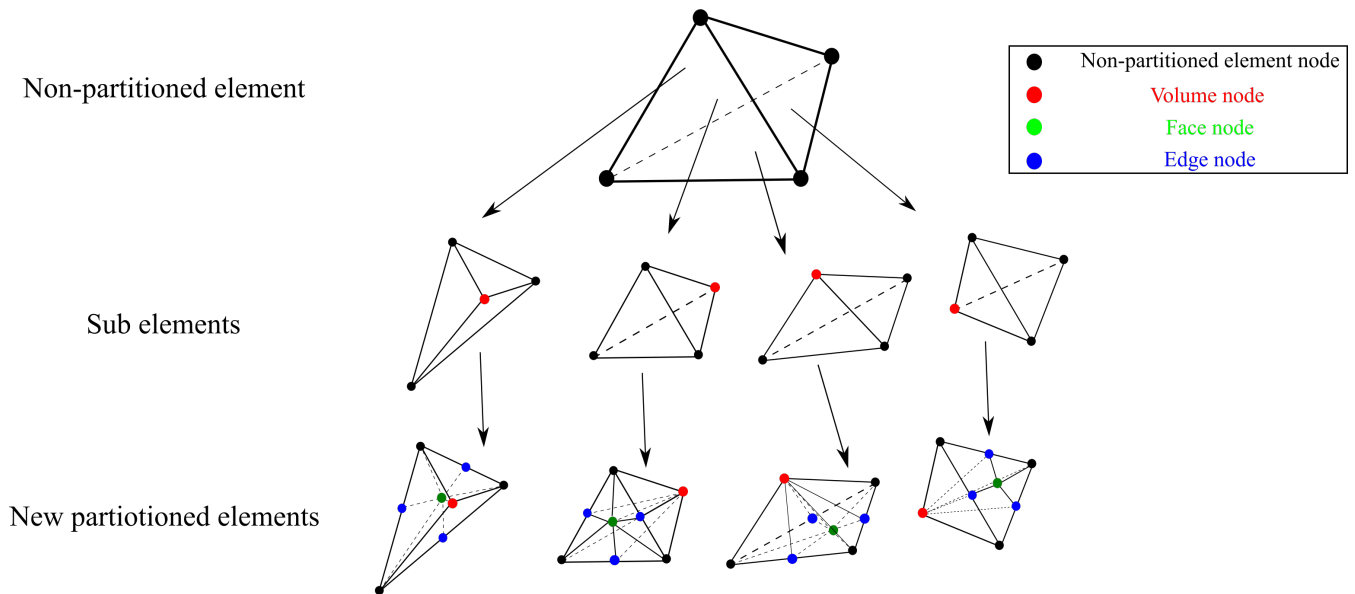
In this step, the mesh topology is modified in order to insert new nodes at the identified locations of the crack surface intersection. A local partitioning strategy is used in order to fit the identified crack surface within the mesh topology, i.e., new nodes are added in the locations of the intersection between the crack surfaces and the mesh. Assuming that the six edges of an initial non-partitioned tetrahedron are intersected by the crack, the sequence of operations that are carried out is explained in Fig. 6 as follows:

(i). the intersected non-partitioned element can be partitioned into four sub elements connected by a volume node where edge nodes are inserted at the positions of the crack intersection with the edges. The position of the volume node is calculated to be at the center of the crack surface that passes through the non-partitioned tetrahedron, i.e., its coordinates are calculated as the average of the coordinates of edge nodes.

(ii). additional face nodes are added on each face of the tetrahedron. The face nodes are added in order to ensure a unique partitioning scheme and to eliminate the possibility of having more than one admissible partitioning scheme as illustrated in Fig. 7. If two intersections are identified on one face, there will be two possibilities for the new mesh configuration. On the other hand, adding a face node gives a unique mesh topology. Although it is not the scope of this paper, it is worth mentioning that the unique partitioning strategy is also suitable for our parallelization strategy where a SMPD (single program on multiple data) [34] is used. Using this strategy, every processor contains a partition of elements in the mesh in which the interface nodes are shared between the neighbouring partitions. The uniqueness of the partitioning strategy helps in getting rid of any ambiguity about the partitioning of the shared elements between different processors. This partitioning strategy leads to a total number of 24 new partitioned elements where all the added nodes lie on the crack surface.

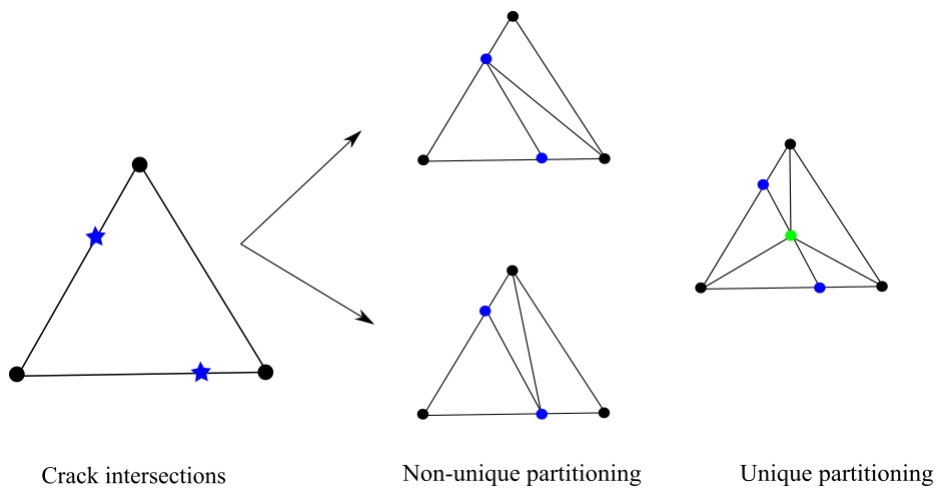
In practice, the number of crack intersections for each edge in the mesh depends on the detected crack path. Therefore, the next step is to merge the edges that do not contain any intersection so that the two elements sharing these edges are compacted to one element. In addition, for the face that does not have any intersections on one of the edges, all the elements sharing this face are compacted to form only one element. The final topology of the patch will only have edge and face nodes where there is at least one edge intersection on the face.

## Mesh partitioning strategy

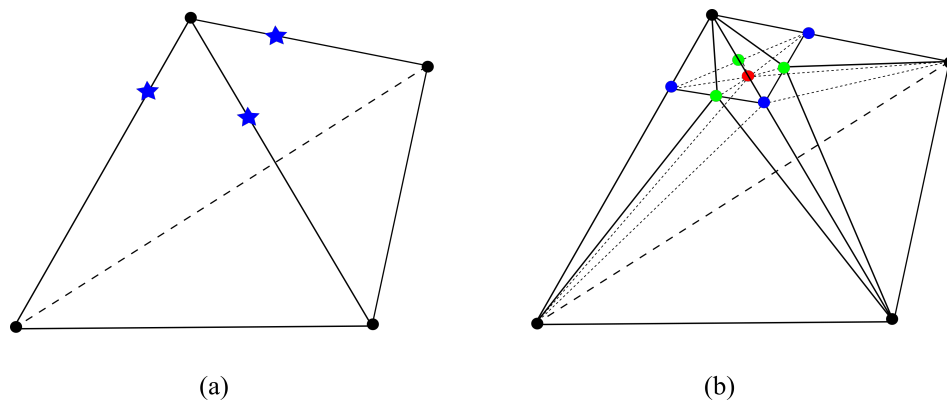


**Figure 6:** Mesh partitioning strategy used to fit the crack surface with the mesh.

In Fig. 8a, three intersections have been identified, the topology of the new partitioned elements is shown in Fig. 8b where the coordinates of face and element nodes are calculated according to the mentioned rules. Six crack faces are identified in this configuration where each face contains an edge node, face node and the volume node. The next step is the duplication of nodes that belong to the crack faces in order to open the crack surfaces. It can be seen that each partitioned element cannot have more than one crack face by construction. This feature is very important as it leads to a unique description of the crack surface in the case of crack bifurcation.



**Figure 7:** A comparison between the unique and face partitioning schemes.



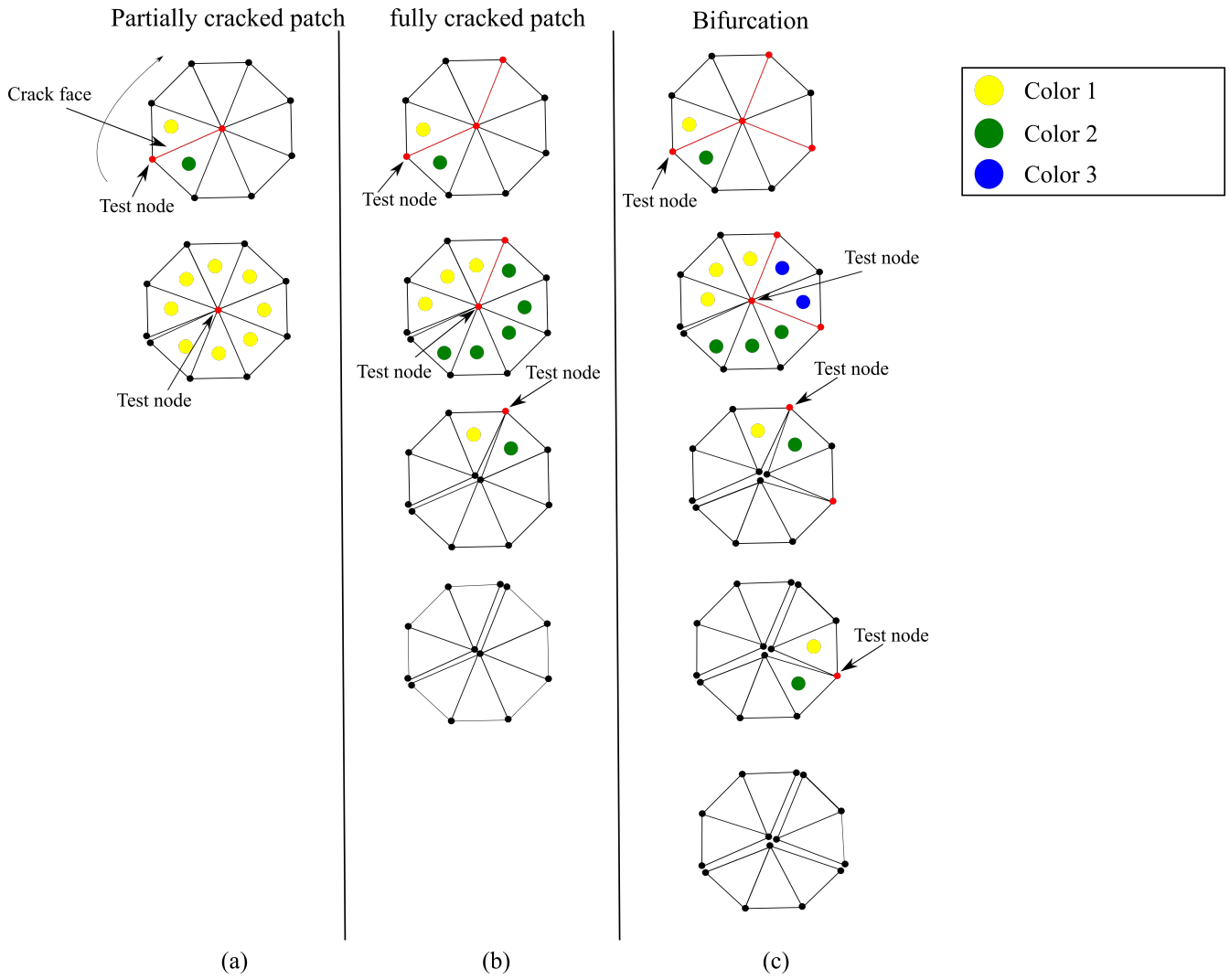
**Figure 8:** The strategy of identifying the crack faces

Fig. 10b shows how the mesh topology is modified in order to fit the crack surface within the mesh.

### 3.4. Nodal duplication by virtual non-manifold patch repair

In this part, the nodes that belong to the crack surfaces should be duplicated. The aim of this step is to open the crack surfaces in order to simulate the decohesion process. Once a crack face is identified within a manifold patch, it becomes a non-manifold in the sense that it becomes a non-continuous patch. The graph coloring algorithm widely used in the graph theory is adopted for this purpose. In graph coloring, a vertex or face is assigned a unique color so that no adjacent one can have the same color, see [29]. In our case, the patch around each node that needs to be duplicated is analyzed. Each connected patch of elements should have the same color. The color is changed once a crack face separates two patches. Finally, each node is duplicated according to the number of colors associated to the patches connected to it.

In order to illustrate the algorithm, Fig. 9 shows three mesh patches of triangular elements in 2D showing the three possible scenarios of nodal duplication (the generalization to 3D is straightforward). A crack face is identified as the surface that connects two nodes (three nodes for a tetrahedral element in 3D) as described by the sequence agnostic partitioning strategy. In the first patch 9a, one crack face is identified which leads to a partially cracked patch. Starting with a loop around a test node, two elements are connected to the node having a crack face in common. Each element takes a different color leading to two copies of this node, one copy for each disconnected patch. The second test node is not duplicated since all the attached elements have the same color, so it represents the crack tip. The second patch as shown in Fig. 9b contains two crack faces. This results in having two copies of the first test node leading to a crack opening in the initial patch. Then, a second test node will also have two copies leading to a second opening of the crack surfaces in the patch. The last test node is then duplicated in order to totally separate the two patches leading to a fully cracked patch. A third patch shown in Fig. 9c contains three crack faces leading to a bifurcation of the crack path. These faces contain four nodes that lie on the crack surface. Starting with an initial test node, the same initial crack path is obtained as the partially and fully cracked patches. However, the analysis of the second node leads to three different colors since there are two crack faces. Hence, three copies are made of this central node. Finally, the third and fourth test nodes are duplicated to two copies leading to a final crack bifurcation.



**Figure 9:** Illustration of the use of the coloring algorithm for the nodal duplication

Fig. 10c shows an example of the use of the coloring algorithm for the nodal duplication and the opening of the crack surfaces.

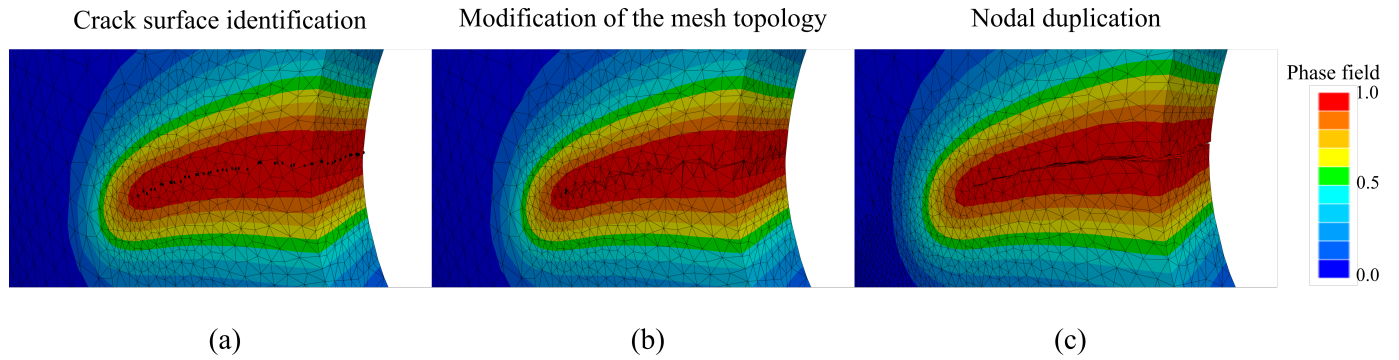


**Figure 10:** Illustration of the main operations of the crack insertion algorithm. Crack identification in (a), mesh modification in (b) and nodal duplication followed by volumetric remeshing in (c).

### 3.5. Summary

A summary of the developed method is presented in flowchart in Fig. 11.

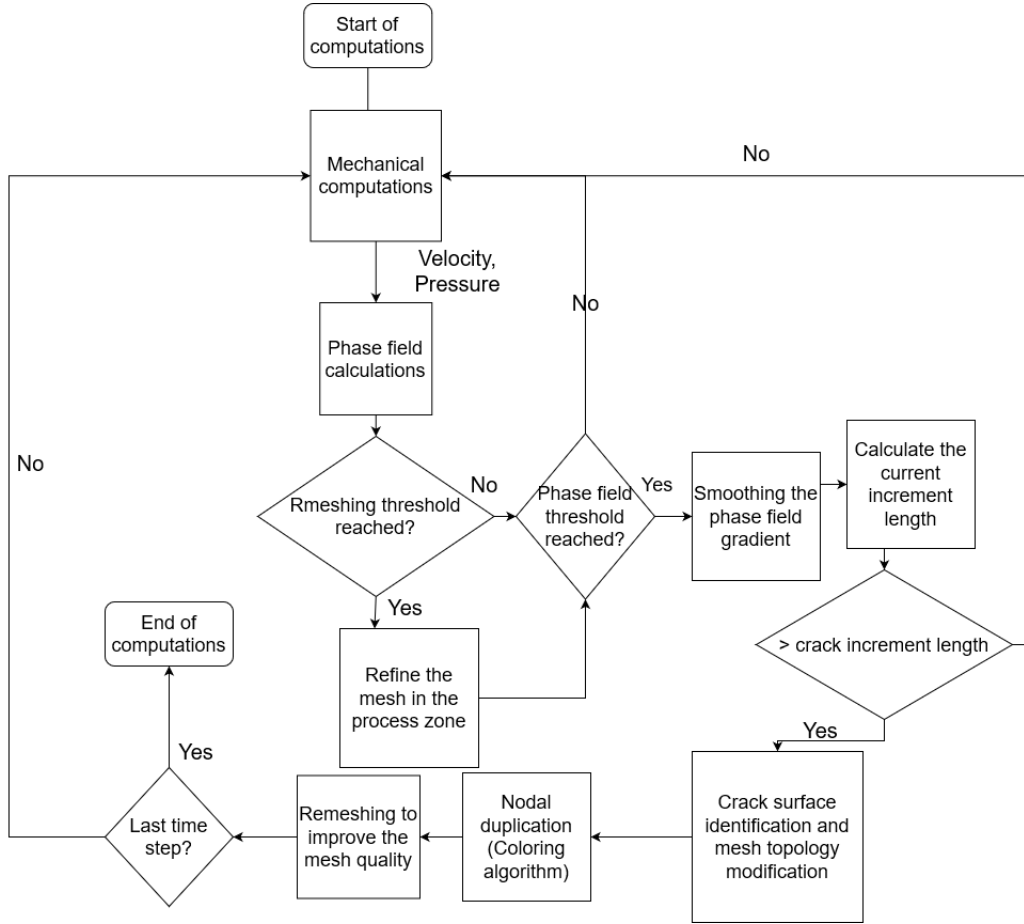


**Figure 11:** Flow chart of the crack insertion algorithm CIPFAR.

## 4. Numerical examples

In this section, three numerical examples are presented in order to show the ability of the developed algorithm to describe the crack initiation and propagation. All the mechanical and phase field computations are carried out using tetrahedral elements. The staggered algorithm [35] is used in order to decouple the mechanical and phase field equations (more details are found in appendix A).

### 4.1. Double notched symmetric specimen

In this example, first mode of ductile fracture is demonstrated using a symmetric specimen with double notches subjected to tensile loading. Fig. 12 shows the geometry and boundary conditions of the specimen where the thickness is 1 mm. A linear hardening law described in eq. 9a is used. The material and model parameters are as follows:  $E = 200$  GPa,  $\nu = 0.3$ ,  $\sigma_0 = 300$  MPa,  $H = 600$  MPa,  $G_c = 5$  kJ/m<sup>2</sup>,  $\beta_1 = \beta_2 = 1$ , plastic threshold  $W_0 = 5$  MPa and a time step of 0.5 sec until the maximum value of the phase field reaches 0.1 and 0.125 sec for the rest of the

simulation in order to ensure the convergence of the solution. An initial mesh size of 1 mm is used everywhere in the mesh. The mesh is refined in the damaged zone based on the equivalent plastic deformation as described by the adaptive remeshing algorithm in section 2.3. A comparison is done between coarse and fine meshes with the smallest mesh sizes  $h_{min}$  as 0.4 mm, 0.3 mm and 0.2 mm, respectively where length scale  $l_c$  is set as 0.8 mm. The effective crack area  $A_{fixed}$  is set to  $0.5 \text{ mm}^2$  for all the examples.

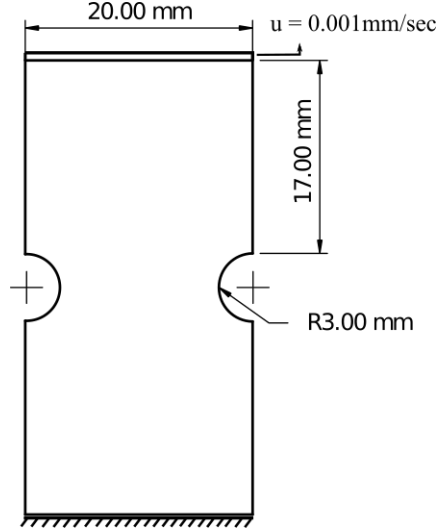


**Figure 12:** Geometry and boundary conditions of a double notched symmetric specimen.

The phase field evolution and discrete crack surfaces propagation at three different displacements are illustrated in Fig. 13 for different mesh sizes. It can be observed that the actual crack path follows the implicit crack path predicted by the evolution of the phase field until the final rupture of the specimen. Although the intermediate crack evolution process is slightly different for the different mesh sizes, the same crack path is obtained at the final rupture for the three mesh sizes. These slight differences can be explained by the increase of the accuracy of mechanical and phase field resolutions with the mesh refinement.

Fig. 14 shows the force vs. displacement curves for different mesh sizes with a comparison between the discrete crack propagation and fixed mesh computations. Two main conclusions can be drawn: (i). a convergence behaviour is observed with the reduction of mesh size which is coherent with the characteristic features of the implicit gradient-based non-local damage formulations; (ii). a numerical diffusion due to remeshing is also observed for the discrete crack propagation cases, however, a similar convergence behaviour with the reduction of mesh size is observed as the fixed mesh computations. It should be noted that the slight deviations from the equilibrium path after each remeshing step leads to a final deviation in the force vs. displacement curve. This numerical diffusion is due to the transport of mechanical fields after each remeshing operation.

The effect of adaptive remeshing threshold on the force vs. displacement curves is shown in Fig. 15 with a comparison with the fixed mesh computations without neither adaptive remeshing nor discrete crack propagation. It can be shown that when the remeshing threshold is reduced, the deviation between the fixed mesh and discrete crack propagation solutions is reduced. This can be explained by the fact that when mesh refinement process is initiated earlier, the mechanical resolution becomes more accurate in capturing the moment of crack initiation. The deviation of

the total strain energy in the case of discrete crack insertion as compared to the fixed mesh case is shown in table 1. In the next presented cases, a remeshing threshold of 0.005 is used.

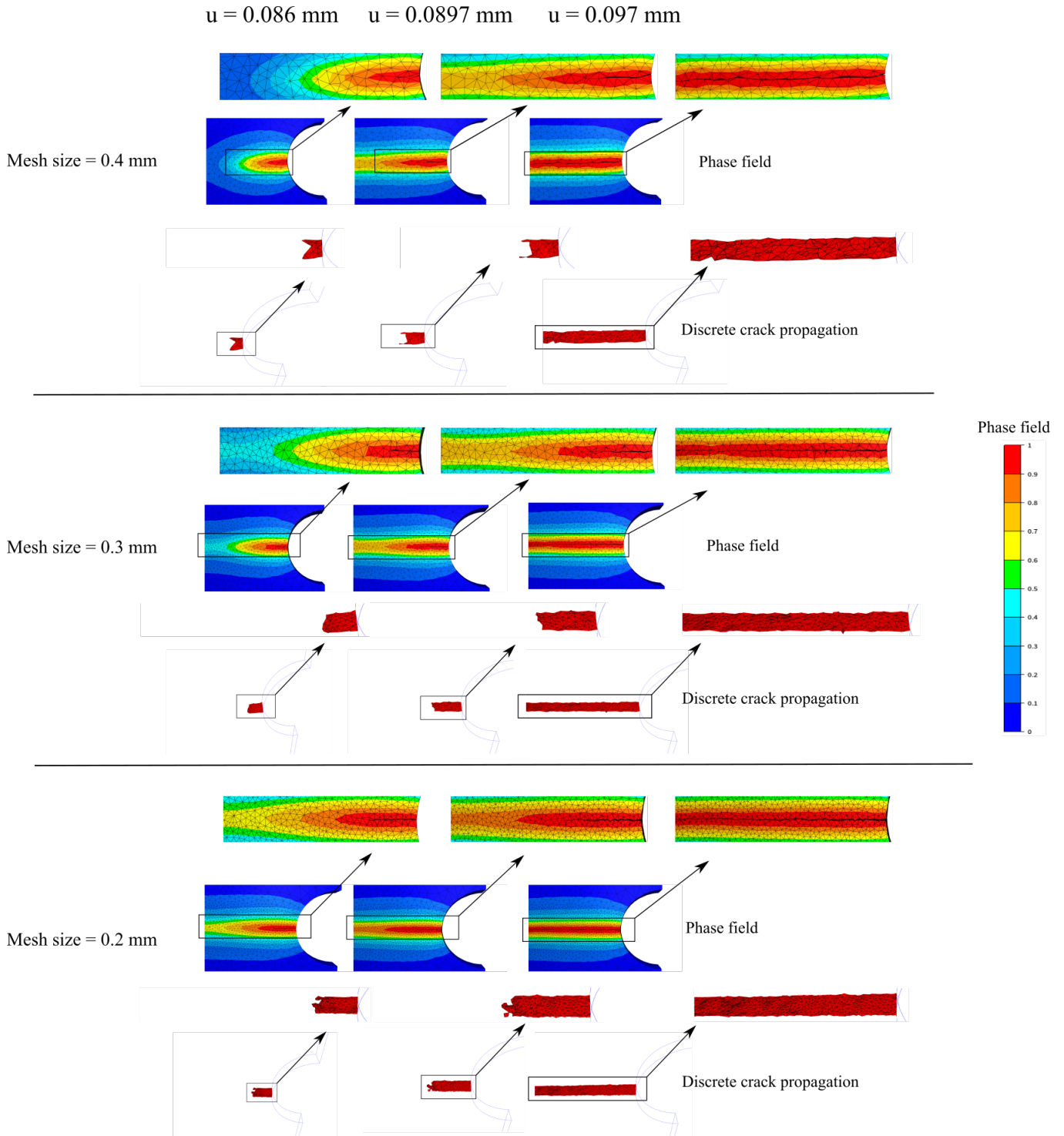


**Figure 13:** Phase field evolution showing the crack initiation and propagation until the final rupture.

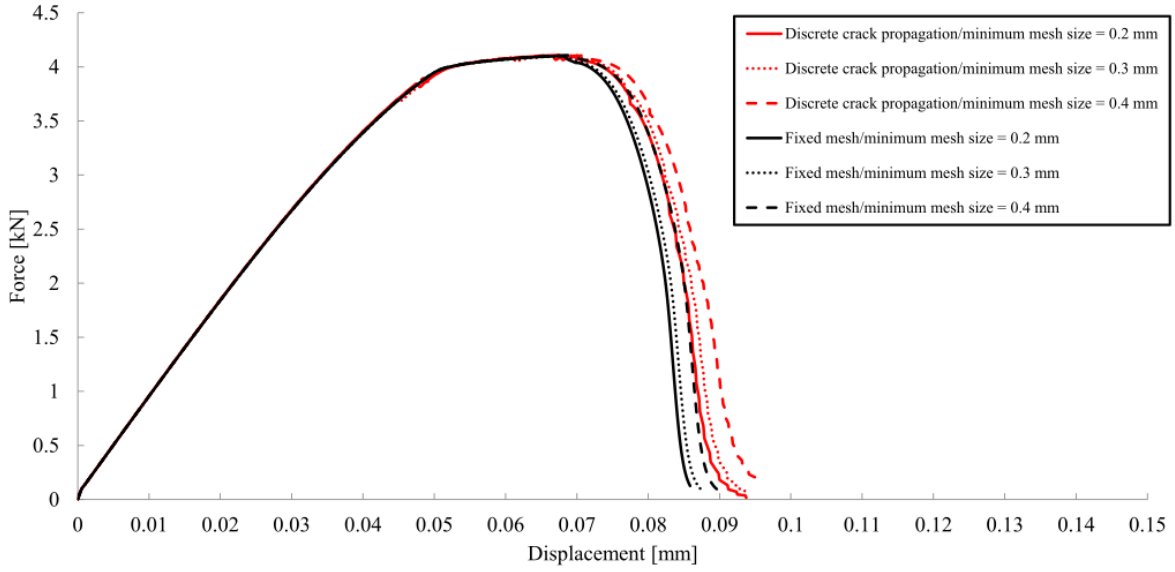


**Figure 14:** Force vs. displacement curves for different mesh sizes with a comparison with the fixed mesh computations.

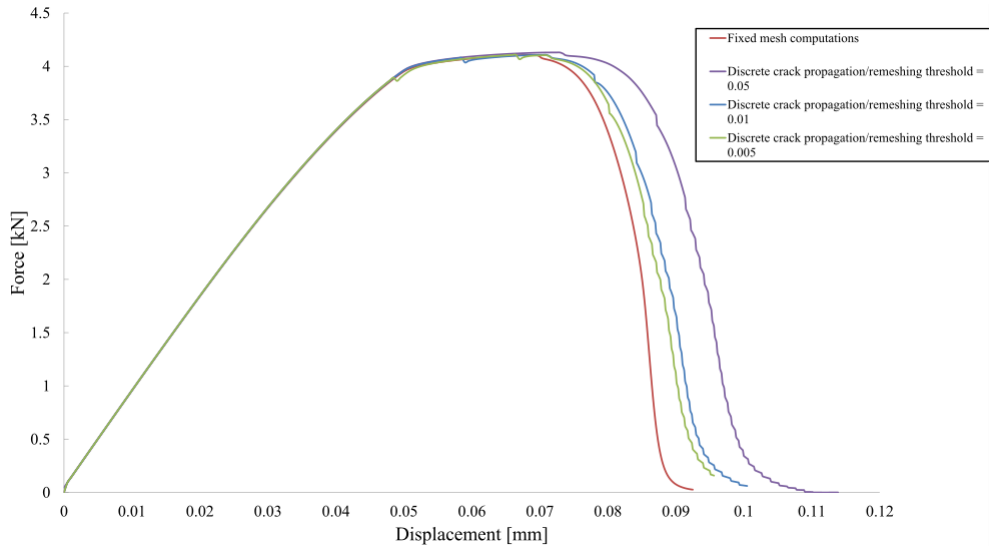


**Figure 15:** Force vs. displacement curves for different remeshing thresholds where the adaptive mesh refinement is based on the equivalent plastic strain.

**Table 1:** The effect of remeshing threshold on the total strain energy

Remeshing threshold	Total strain energy $J$	Deviation %
0.05	0.281	12.75
0.01	0.263	6.67
0.005	0.259	5.1

The effect of crack increment length threshold on the force vs. displacement curves is shown

in Fig. 16. Results are compared with pre-refined fixed mesh computations which is considered as the reference case. It is worth mentioning that the discrete crack insertion has a negligible effect on the mechanical resolution since the material is totally damaged before the insertion of the crack increment. Slight deviations between the curves are observed after the crack initiation moment. This result is directly related to the numerical diffusion that increases with the increase of the number of remeshing operations as shown on the figure. It can be also shown in Fig. 17 that the final crack paths are very similar for the different crack increment lengths. This result is consistent with the fact that the discrete crack path follows the phase field evolution which is independent on the choice of the crack increment length.

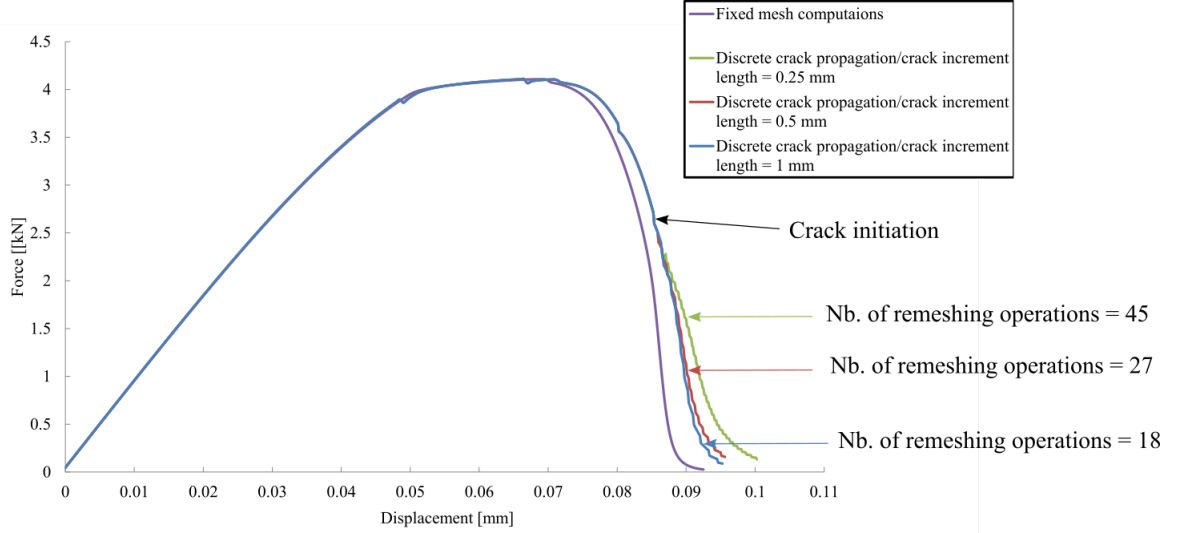


**Figure 16:** Force vs. displacement curves for different crack increment lengths.

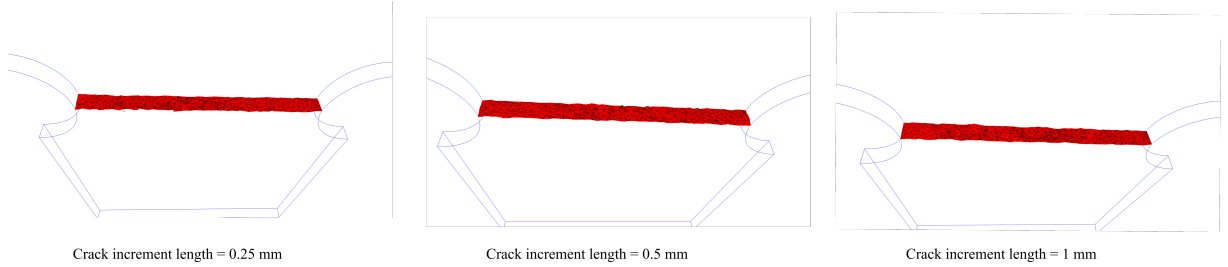


**Figure 17:** Final crack surface for different crack increment lengths.

As suggested in [35], the effect of stress triaxiality  $\eta$  in the prediction of damage localization and hence the crack evolution is important. In order to test this effect, the same proposed modification is added to the plastic energy  $W_p$  that appears in the local history functional by adding a stress triaxiality function  $\phi(\eta)$ . The stress triaxiality is defined as follows  $\eta = \frac{-p}{\|s\|}$ . The rate form of the plastic strain energy becomes as follows

$$\dot{W}_p^{eff} = \frac{\dot{W}_p}{\phi(\eta)} \quad (25)$$

where  $W_p^{eff}$  is the effective plastic energy. For the sake of demonstration, the same form and parameters of the triaxiality function are taken as mentioned in the reference [35] which is shown

as follows

$$\phi(\eta) = d_1 + d_2 e^{d_3 \eta} \quad (26)$$

with  $d_1 = 0.1$ ,  $d_2 = 3.8$  and  $d_3 = -1.8$ .

Fig. 18 shows the phase field evolution and discrete crack surface propagation with and without the effect of stress triaxiality, in other words, without adding the stress triaxiality function. All the material and model parameters are fixed for both cases except the effect of the stress triaxiality. When the effect of stress triaxiality is added, it can be shown that the internal crack initiation occurs far from the notch boundary which is the location of maximum stress triaxiality. The same result was observed in [35] which was also qualitatively confirmed by the experimental observations reported in [36].

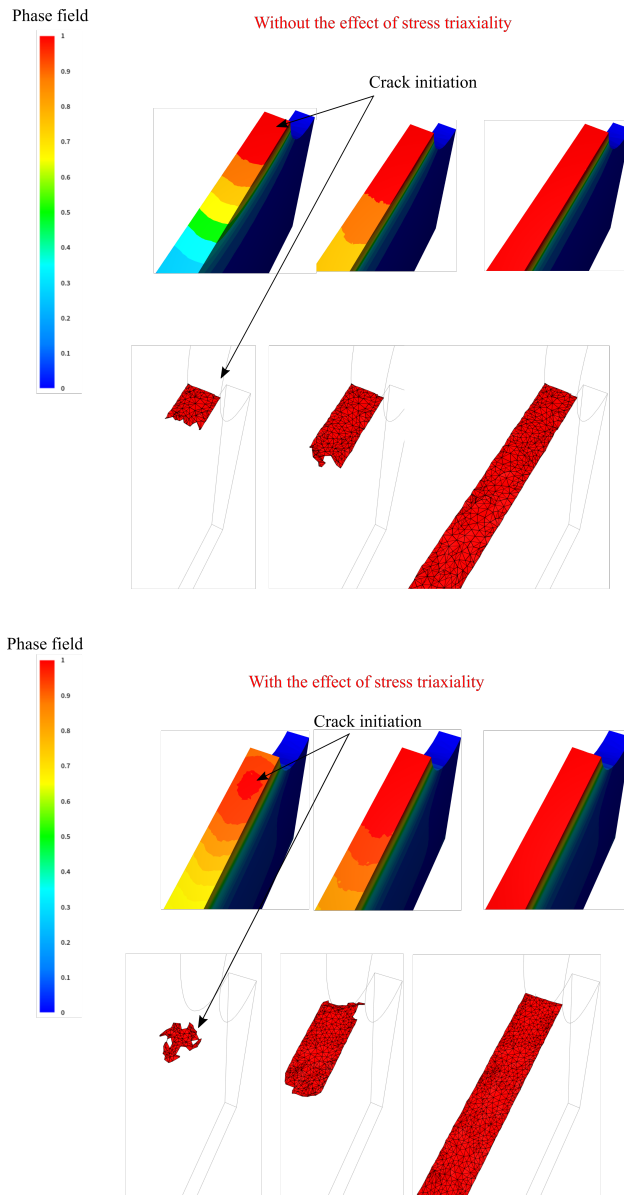


**Figure 18:** The effect of triaxiality function on the initiation and propagation of discrete crack surface.

The developed algorithm is able to describe the full cracking process starting with the initiation at the expected locations until the formation of the complete crack surface leading to the separation

of the initial specimen into two pieces. In addition, the final crack paths are independent on the mesh size given that the mesh size is small enough for a good resolution of the phase field equations.

#### 4.2. Double notched asymmetric specimen

In this example, a mixed mode fracture is simulated in order to prove the ability of the algorithm to deal with complex cracking pattern with multiple initiation sites. The geometry and boundary condition along with the initial mesh are shown in Fig. 19 as in [5, 9]. The initial mesh size is set to 0.4 mm. Using the adaptive remeshing algorithm, the mesh size is reduced in the regions where the crack is expected to propagate where the equivalent plastic strain is used as an indicator function with a threshold of 0.01. A linear hardening law described in 9a is used. The material parameters are :  $E = 180$  GPa,  $\nu = 0.28$ ,  $H = 300$  MPa,  $\sigma_0 = 443$  MPa. The model parameters are:  $l_c = 0.4$  mm,  $\beta_1 = 0$  and  $\beta_2 = 1$ . The other model parameters  $G_c$  and  $W_0$  are varied in order to show their effect on the phase field evolution.

The time step is set to 0.01 sec in the beginning of the simulation until and then reduced to a minimum time step  $\Delta t_{min}$  once the maximum value of the phase field reaches 0.1. A time step convergence study is shown in Fig. 20 with the following model parameters  $G_c = 5$  kJ/m<sup>2</sup> and  $W_0 = 10$  MPa. A convergence behaviour is observed with respect to the time step most notably for the values less than 0.00625 sec which will be used in all the following simulations. The crack increment length is fixed at 0.5 mm in all the presented examples.

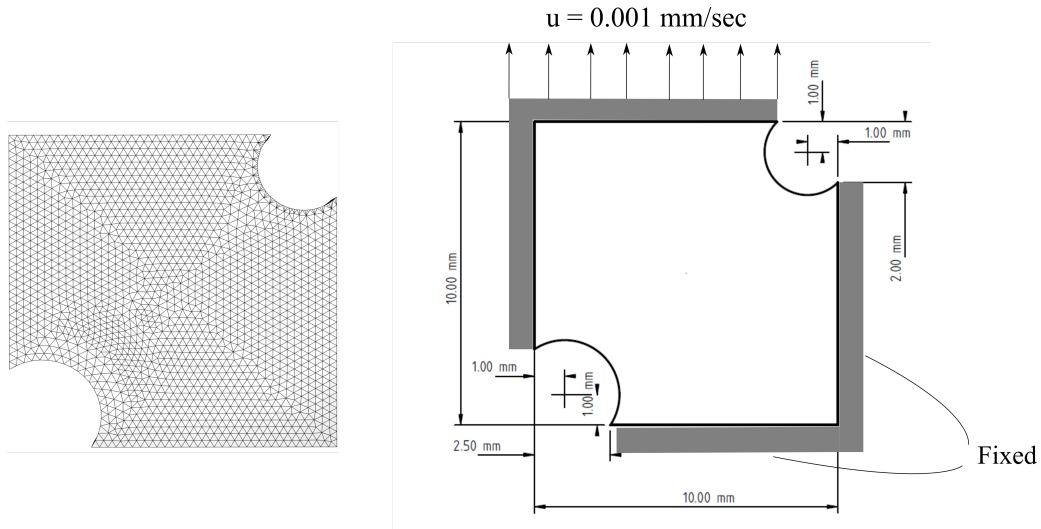


**Figure 19:** The geometry and boundary conditions along with the mesh of an asymmetric double notched specimen. The thickness of the specimen is set to 1 mm.

Figures 21 and 22 show the phase field evolution and discrete crack surface propagation at three different displacements for coarse and fine meshes of element sizes of 0.2 mm and 0.05 mm, respectively. From a global point of view, it can be shown that the crack initiation and propagation in both cases are very similar. However, a better resolution of the quality of the crack surface is observed with the fine mesh. This result is coherent with the fact the the order of approximation of the crack surfaces prediction follows the order of finite element approximation where linear elements are adopted in this study. Fig. 23 shows the force vs. displacement curves for three different mesh sizes where a convergence behaviour is observed when the mesh is sufficiently refined.

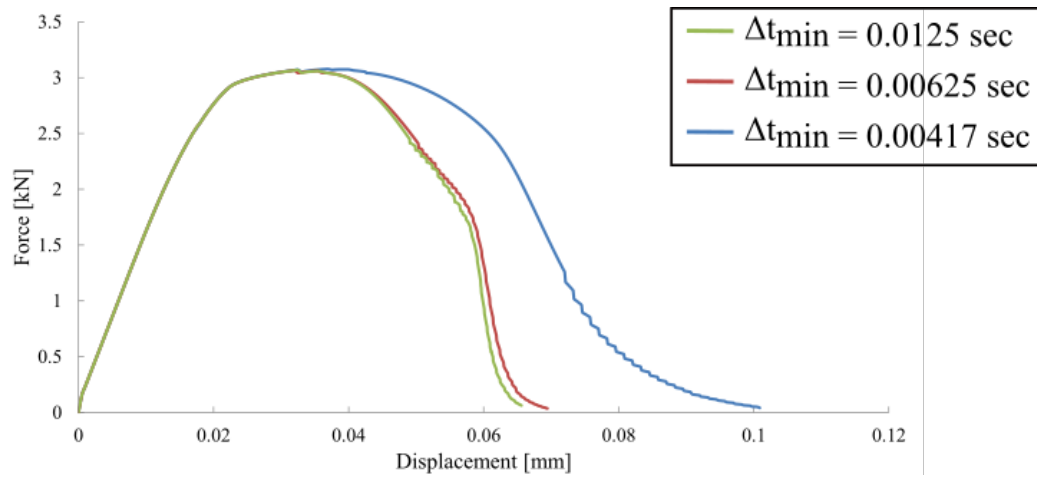


**Figure 20:** Convergence of the Force vs. displacement curve with respect to the reduction in the time step.

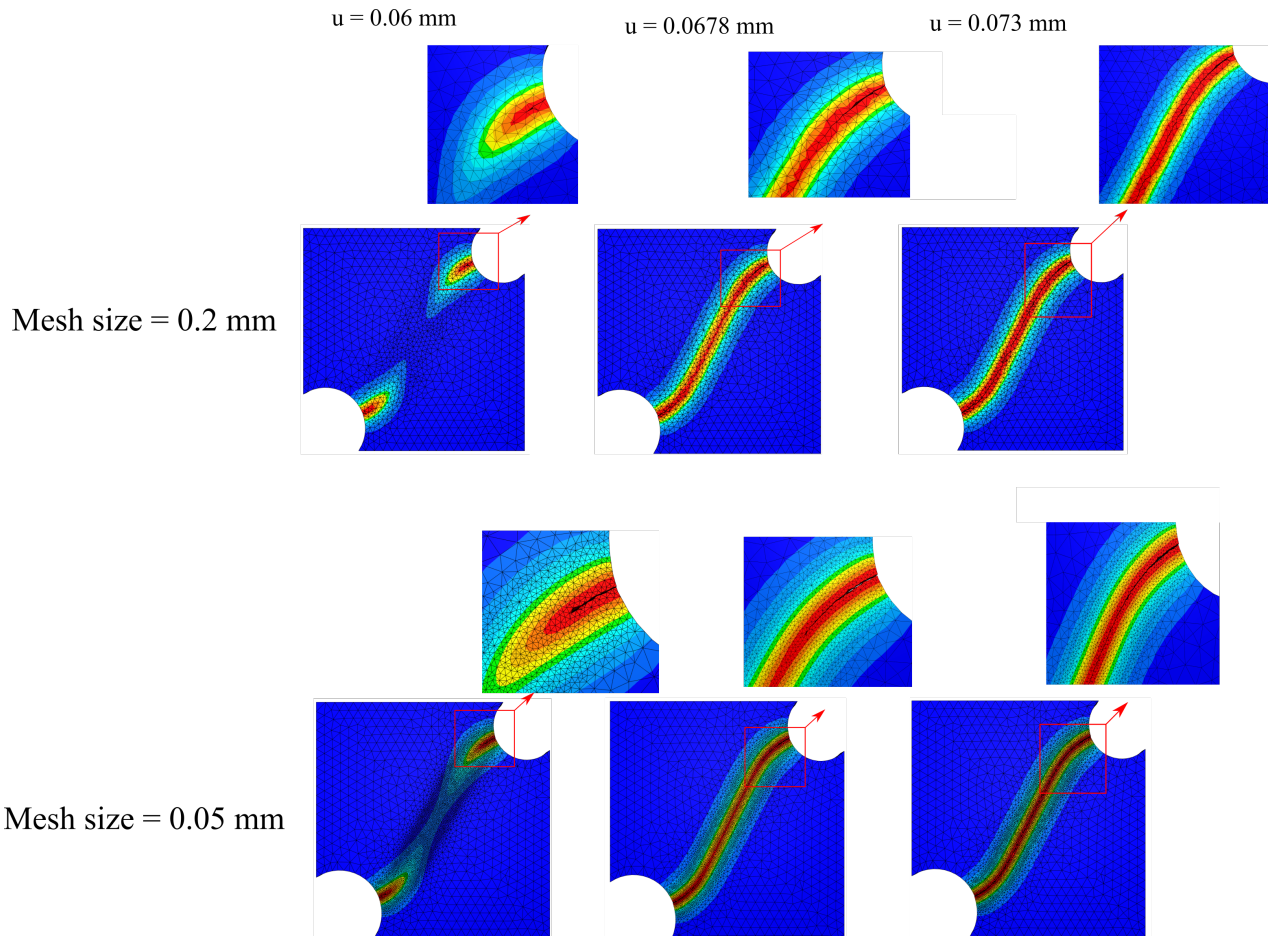


**Figure 21:** Phase field evolution accompanied with the crack path propagation at three different displacements using two different mesh sizes.

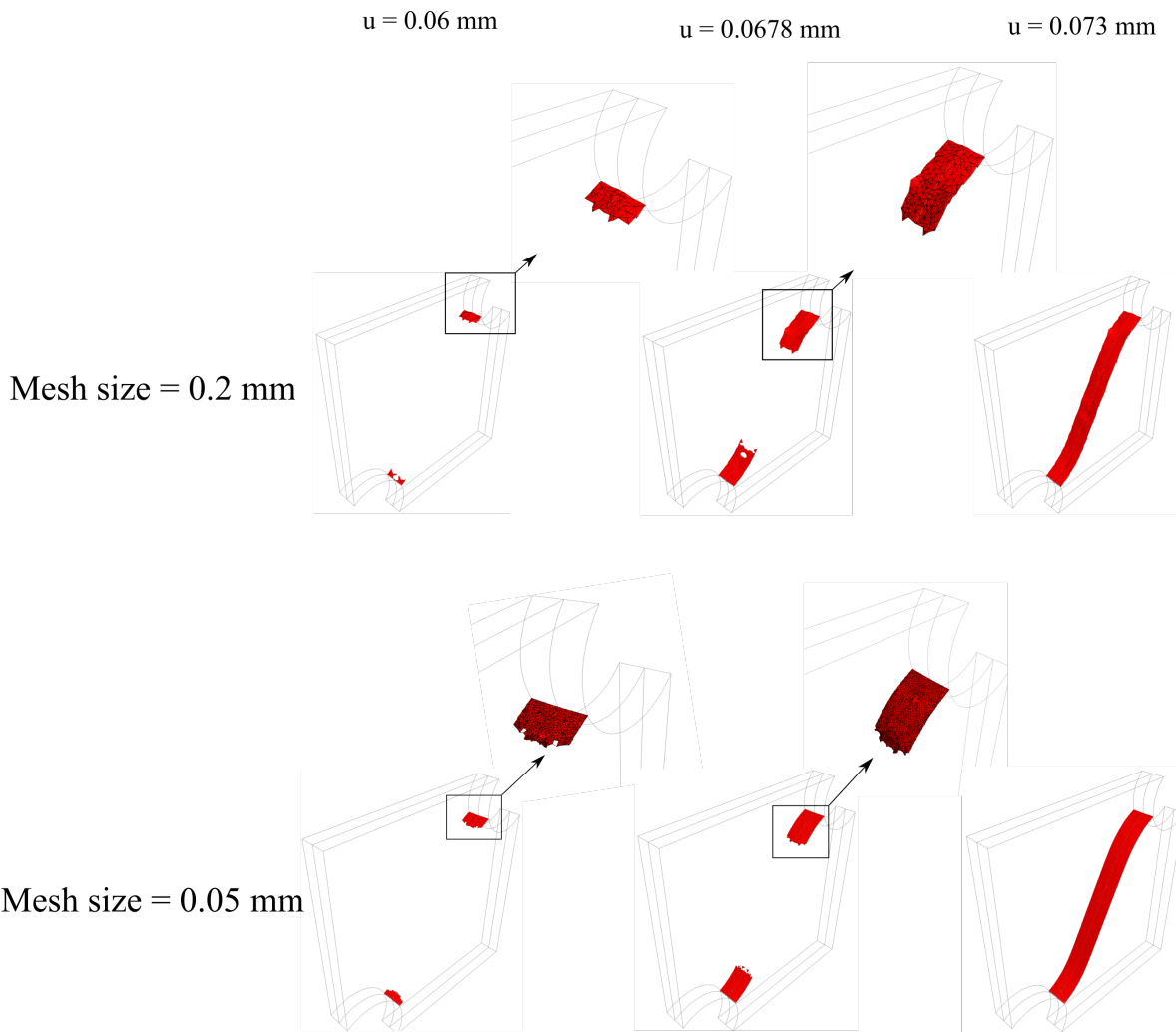


**Figure 22:** Crack surfaces evolution in 3D at three different displacements using two different mesh sizes.

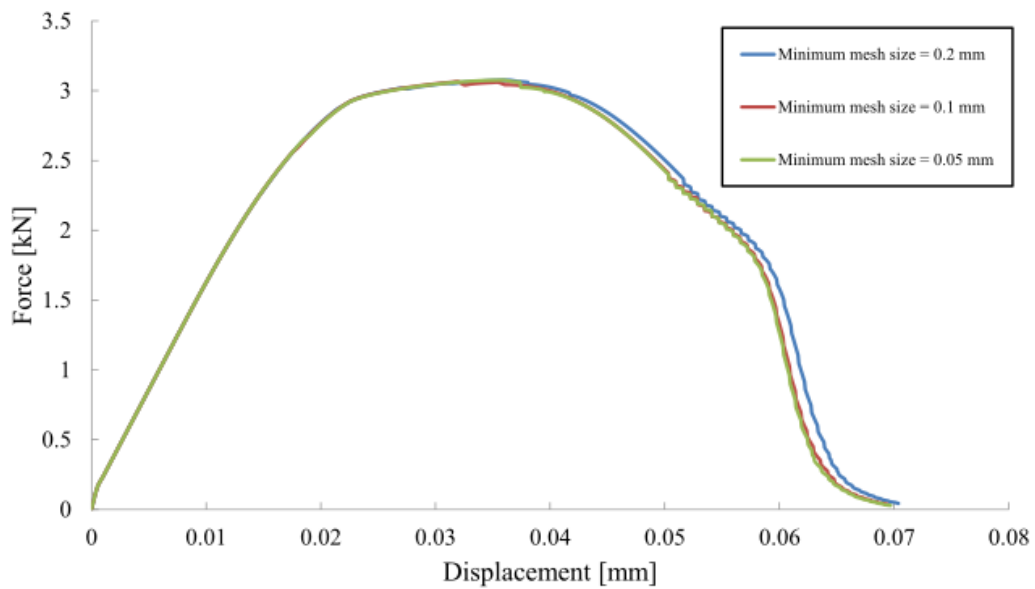


**Figure 23:** A comparison between three mesh sizes on the Force vs. displacement curves.

Fig. 24 shows the effect of stress triaxiality on the initiation of the phase field and hence the discrete crack surface at different values of the plastic threshold  $W_0$ . The phase field profile is shown at a cross section that cuts the upper notch of the specimen. The same modification to the local history functional  $\mathcal{H}$  as in 4.1 is done by adding a stress triaxiality function  $\phi(\eta)$ . It is clear that without adding the effect of stress triaxiality, the crack is always initiated at the boundary of the upper notch. On the other hand, an internal crack is initiated far from the notch boundary which follows the onset of crack initiation predicted by the phase field evolution. The force vs. displacement curves that show the effect of plastic threshold  $W_0$  on the results are plotted in Fig. 25 where the effect of the parameter on the delay of crack initiation point is clearly demonstrated.

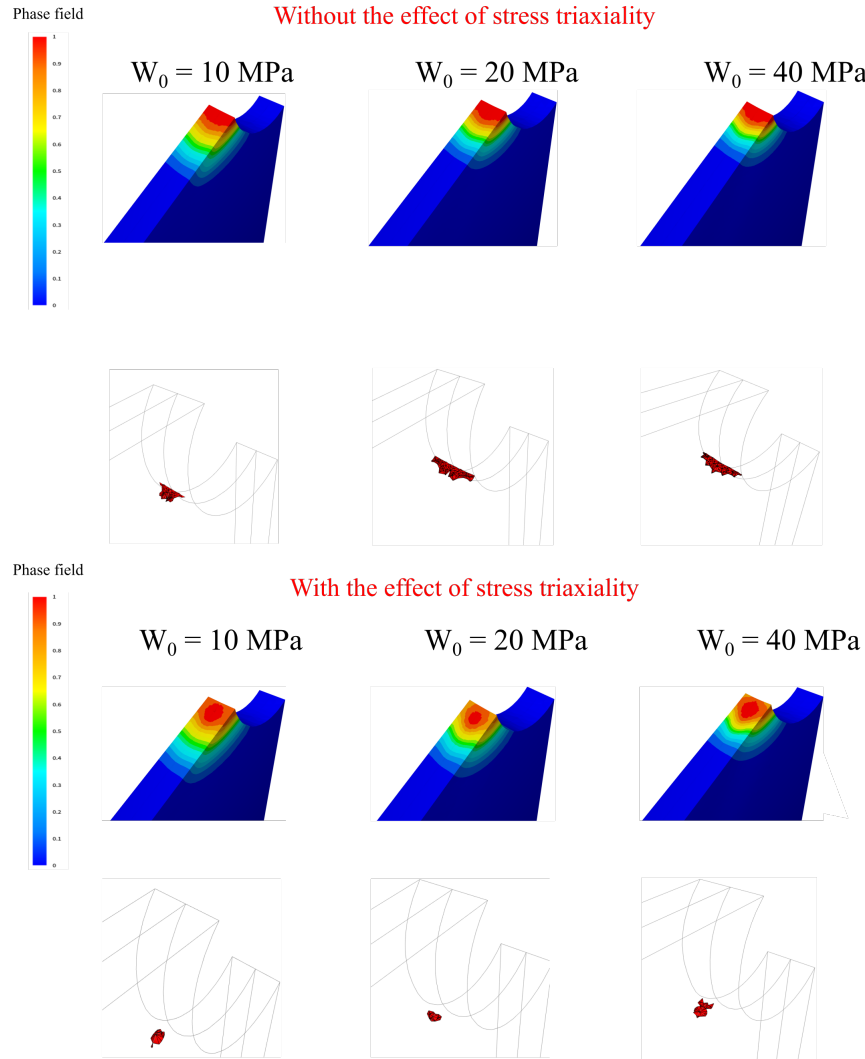


**Figure 24:** The crack initiation at different values of the plastic threshold  $W_0$ . Results are shown without the effect of stress triaxiality (up) and with the effect of stress triaxiality (bottom).

$$G_c = 5 \text{ kJ/m}^2$$

Without the effect of stress triaxiality

With the effect of stress triaxiality

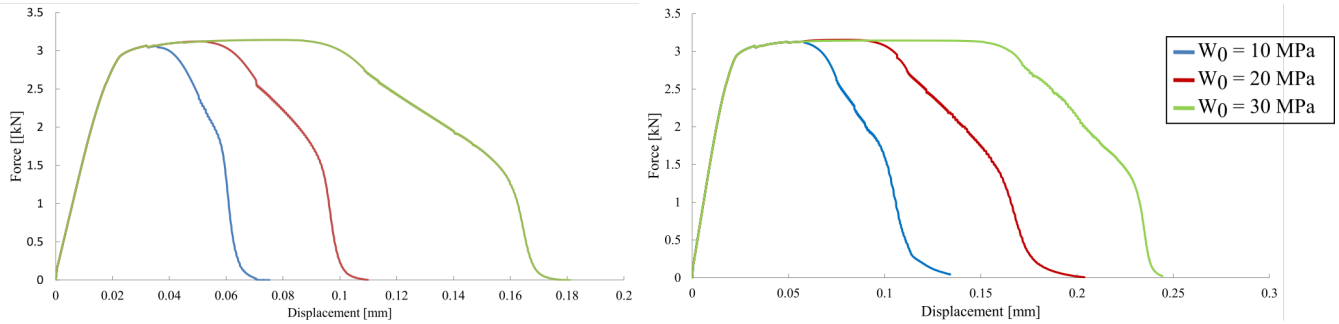


**Figure 25:** The force vs. displacement curves for different values of the plastic threshold  $W_0$ .

Another study is carried out in order to see the effect of the fracture toughness  $G_c$  on the onset of crack initiation. Fig. 26 shows the force vs. displacement curves for different values of  $G_c$  where crack initiation moments are identified by the arrows. It can be shown that when the value of the fracture toughness increases, which is typical in ductile materials, the crack initiation is delayed which is in contrast to brittle materials where the crack initiation happens just after reaching the peak stress. This can be explained by the fact that in ductile fracture, the amount of plastic energy dissipation is much larger than the amount of energy needed to create new crack surfaces. In other words, the crack is initiated at a high plastic strain level. In the current phase field model, this feature is related to the degradation of the yielding surface that appears in eq. 7b so that the phase field evolution is dominated by the plastic strains. These results are confirmed with the experimental tests shown in [36]. Fig. 27 shows the final discrete crack paths obtained for different values of the fracture toughness. The main observation is that the crack path becomes straight for the ductile fracture patterns .i.e., when  $G_c$  increases. This can be explained by the fact that ductile materials fail in the zones of high plastic deformation which is the zone that connects the two notches by a straight line.

$$W_0 = 10 \text{ MPa}$$

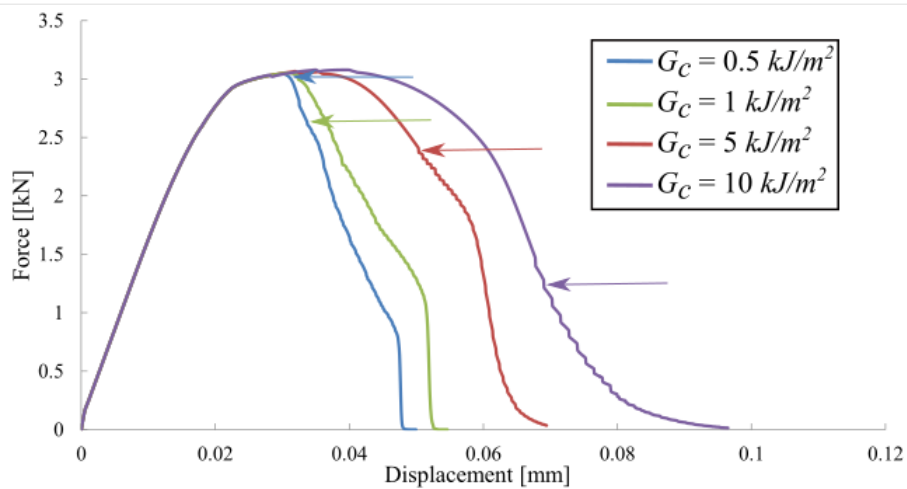


**Figure 26:** The force vs. displacement curves for different values of fracture toughness showing the onset of crack initiation using the crack insertion algorithm.

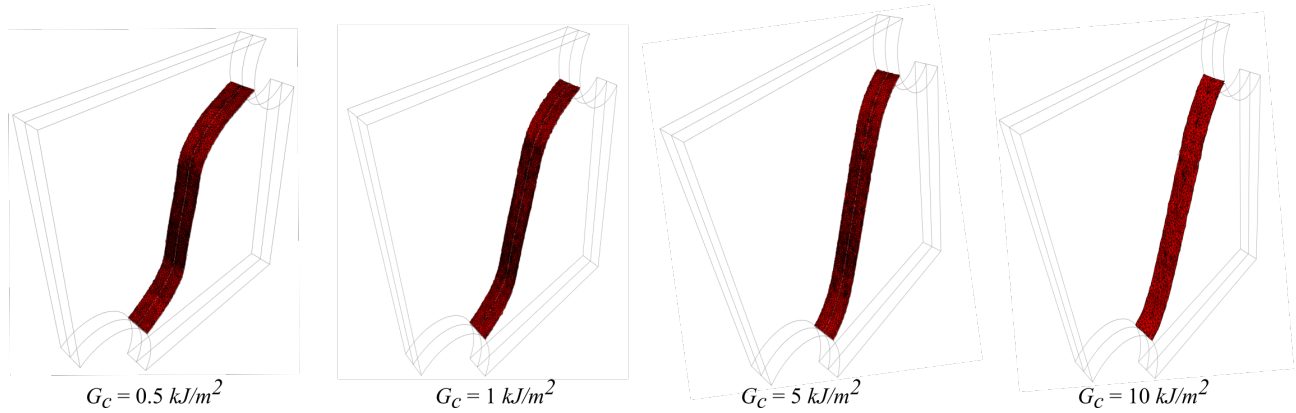


**Figure 27:** The final crack path obtained for different values of fracture toughness  $G_c$ .

The developed strategy serves as an efficient tool in the transition between damage to fracture in ductile materials. The replacement of the crack topology described by the phase field model with a discrete crack in the material. In addition, the degradation of the yielding surface leads to the same mechanical response observed experimentally due to the contribution of the plastic strain in the evolution of the phase field and hence, damaging the material prior to crack initiation.

#### 4.3. Flat tensile specimen

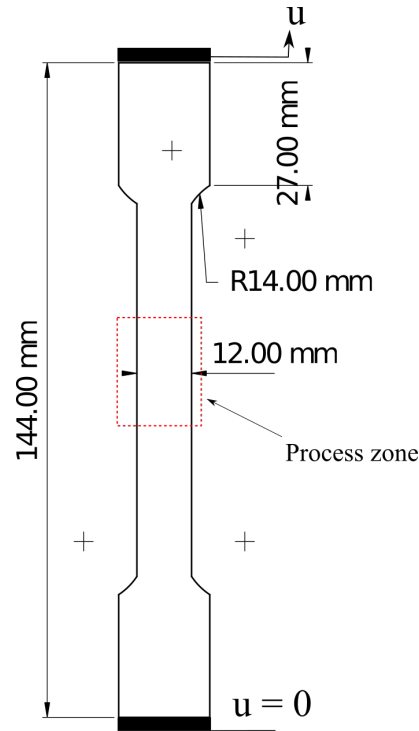
In this example, the crack insertion algorithm is used to predict an internal crack initiation in a flat tensile specimen described in [6]. The geometry and boundary conditions are shown in Fig. 28 where the loading is carried out with a constant velocity of 0.01 mm/sec. A time step of 2 sec is used until the maximum phase field value reaches 0.1 and reduced to 0.4 sec for the rest of the simulation. The effective crack area  $A_{fixed}$  is set to 0.5 mm<sup>2</sup> for all the simulations. A non-linear hardening law described by equation 9b with the material and model parameters presented in table 2 are used. The equivalent plastic strain is used as an indicator function for the mesh refinement with a threshold of 0.05. A fine mesh with smallest element size of 0.25 mm and a coarse mesh with a smallest element size of 0.5 mm are used for the comparison. The characteristic length scale  $l_c$  is set as two times the minimum element length.

Fig 29 where the plastic threshold is set to 10 MPa shows the crack initiation at the center of the specimen which agrees with the experimental observation in [6] shown in Fig. 33. Then, the crack propagates in a direction perpendicular to the loading direction leading to the final failure of the specimen. A final curvature of the crack surface is also confirmed by the experiments. It is clear that the crack surface follows the evolution of the equivalent plastic strain which is expected in ductile fracture. The evolution of the crack surface can also be shown in Fig. 29. A full description of the crack initiation and propagation can be accurately described by the algorithm. Fig. 30 shows the evolution of the phase field along with the crack surface where the plastic threshold is set to 15 MPa. It can be observed the same cracking pattern as in the previous case with a similar evolution of the crack surface in 3D.

The cracking simulation on a coarse mesh is simulated in Fig. 31. The crack is initiated at the center of the specimen where the plastic deformation is localized. However, the final crack path is straight, contrary to what is observed with the fine mesh. The force vs. displacement curves for the three cases can be seen in Fig. 34. The increase in the plastic threshold leads to a crack initiation at a larger displacement.

Finally, another simulation is carried out in order to test the effect of the remeshing indicator function on the cracking process. The phase field is used as an indicator for the mesh refinement process with a threshold of 0.05 and the results are reported in Fig. 31 where a minimum element size of 0.25 mm is obtained in the refined zone. Comparing the results with the results obtained in Fig. 29 shows an inclination in the final crack path. It can be also observed that the evolution of the crack path follows the evolution of the equivalent plastic strain as expected. The reason for this observation is that the phase field evolution starts once the effective plastic exceeds the plastic threshold. In consequence, using the phase field threshold leads to a delay in the mesh refinement in the damaged zone and hence an inaccurate resolution of the plastic strains. This issue has been extensively studied in [28].

The developed algorithm is able to accurately predict the crack initiation location with good agreement with experimental observation. Once the phase field model parameters are well calibrated, a good matching in terms of final crack path and force vs. displacement response with the experiments can be achieved.



**Figure 28:** Geometry and boundary conditions of a flat tensile specimen [6].

**Table 2:** Material and phase field model parameters [6]

Quantity	Value	Unit
Young's modulus, $E$	65200	MPa
Poisson's ratio, $\nu$	0.26	
Yield stress, $\sigma_0$	209.6	MPa
Ultimate strength, $\sigma_\infty$	62.6	MPa
Saturation coefficient, $\delta$	38.81	
Weighing parameters, $\beta_1, \beta_2$	1.0	
Plastic threshold, $W_0$	10/15	MPa
Fracture toughness, $G_c$	50	$kJ/m^2$
Characteristic length scale $l_c$	0.5 or 1.0	mm

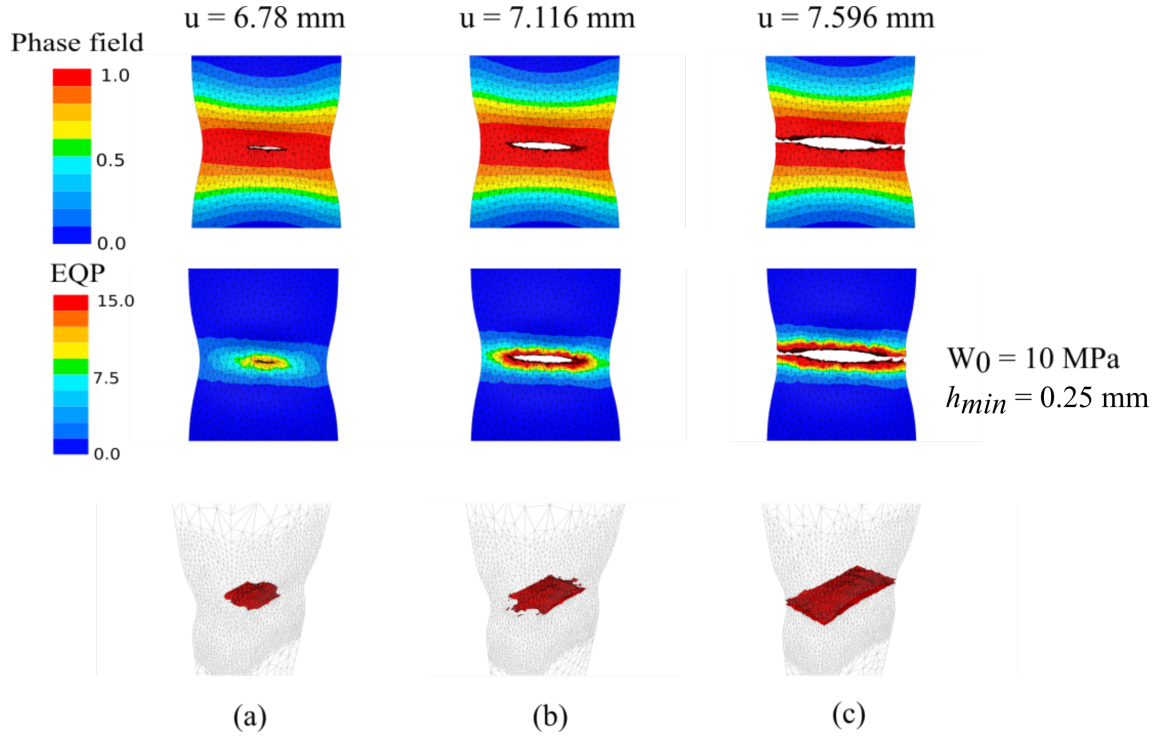


**Figure 29:** The evolution of phase field, equivalent plastic strain (EQP) and the crack surface evolution in 3D at three different different displacements. The initiation, and propagation of the crack are properly predicted where the curvature of the crack lips matches the experimental observations [5]. Minimum element size = 0.25 mm (fine mesh) with a plastic threshold = 10 MPa.

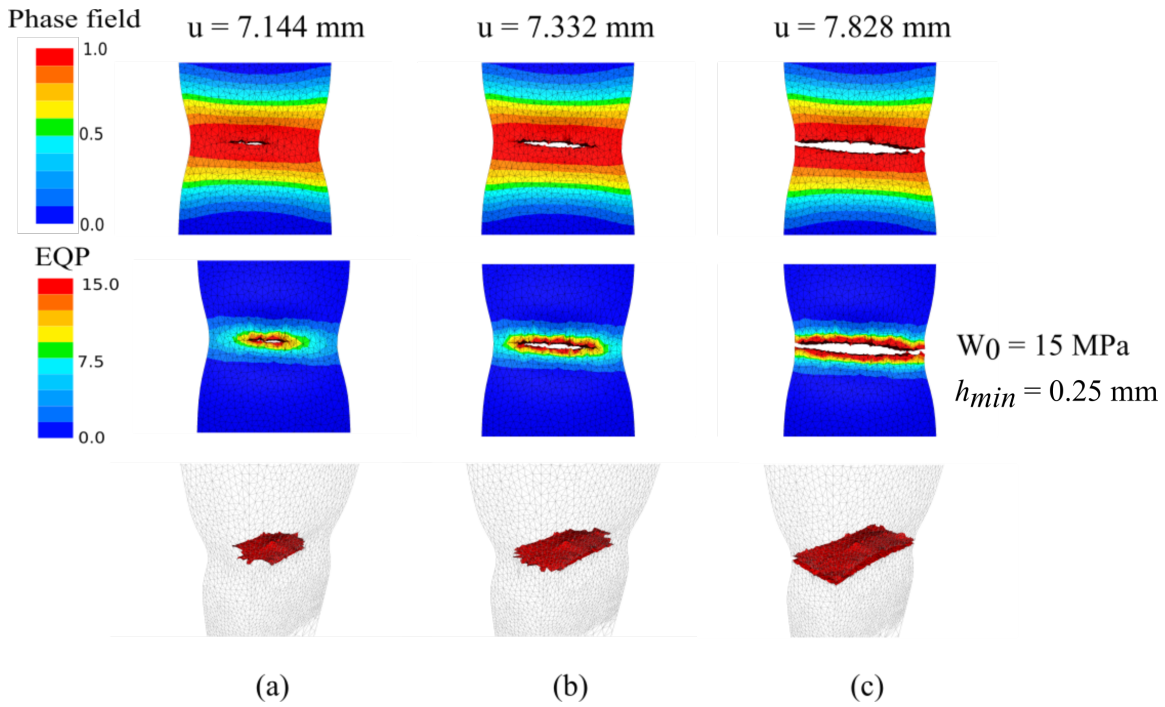


**Figure 30:** The evolution of phase field, equivalent plastic strain (EQP) and the crack surface evolution in 3D at three displacements. The initiation, and propagation of the crack are properly predicted where the curvature of the crack lips matches the experimental observations [5]. Minimum element size = 0.25 mm (fine mesh) with a plastic threshold = 15 MPa.

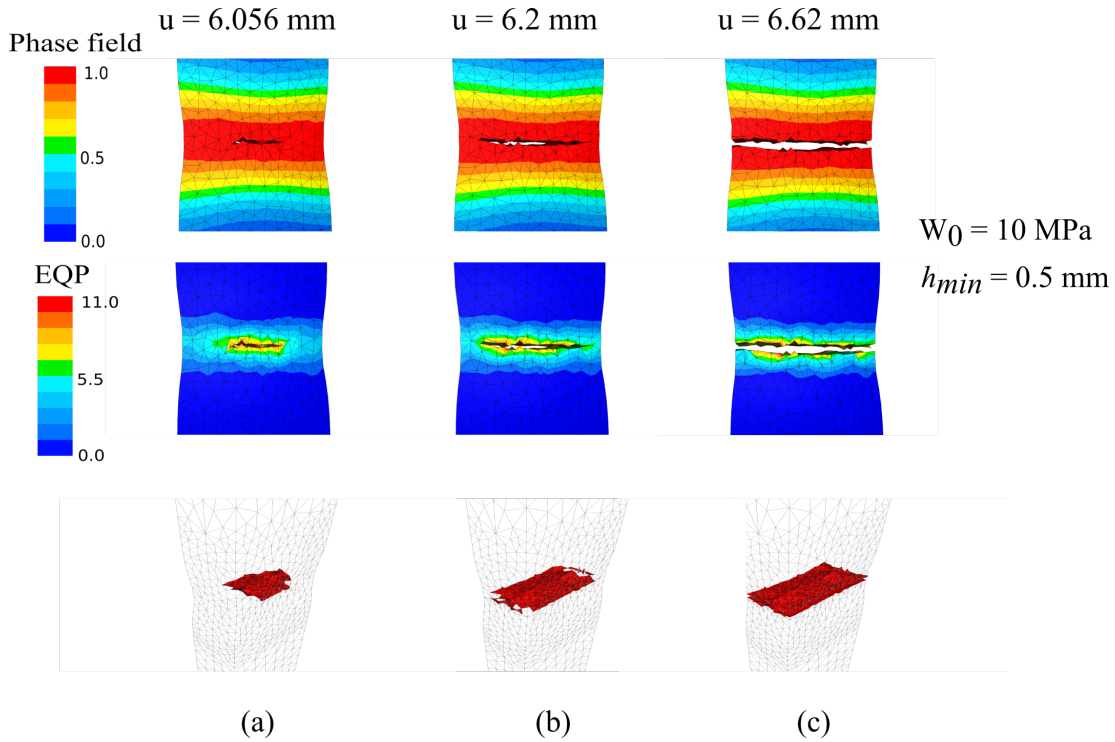


**Figure 31:** The evolution of phase field, equivalent plastic strain (EQP) and the crack surface evolution in 3D at three displacements. The initiation, and propagation of the crack are predicted with less curvature of the crack lips as observed experimentally [6]. Minimum element size = 0.5 mm (Coarse mesh) with a plastic threshold = 10 MPa.

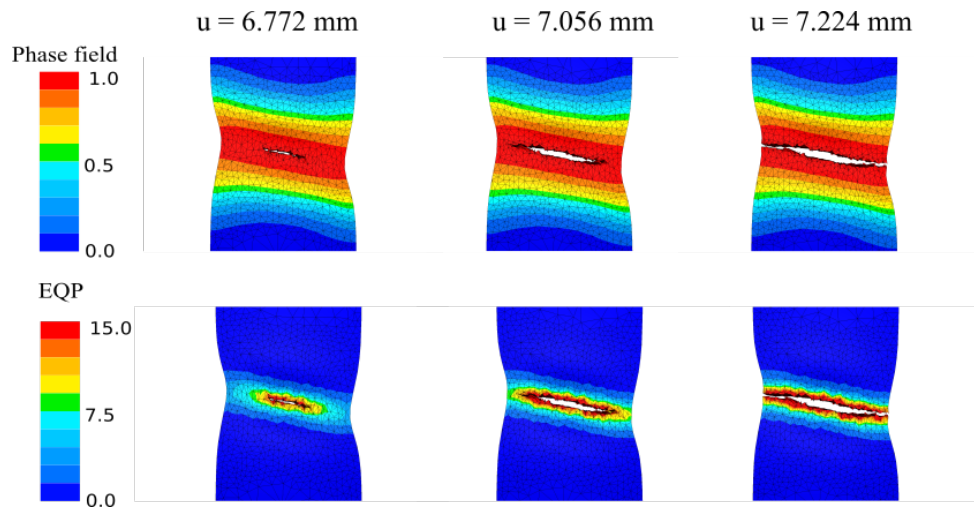


**Figure 32:** The evolution of phase field along with the effective plastic deformation EQP at three different displacements. The phase field is used as an indicator function for the mesh refinement with a threshold of 0.05 as indicated in [28]. The final crack path is inconsistent with the experimental observations reported in [6].

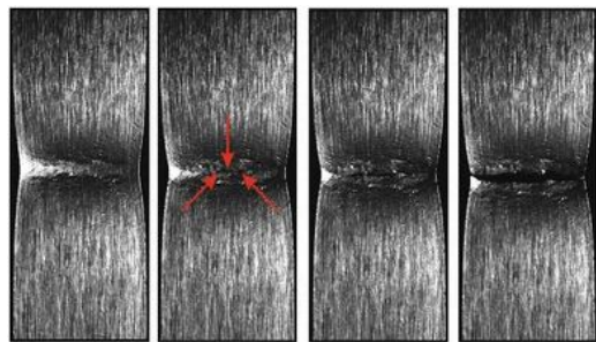


**Figure 33:** Experimental results showing the initiation and propagation of the crack till the final fracture [6]

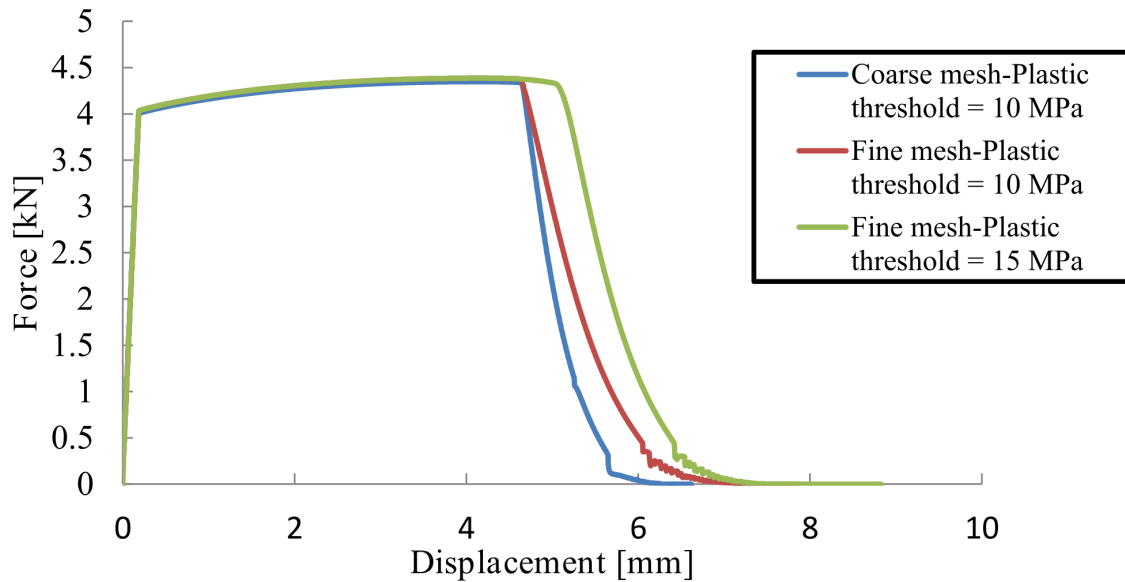


**Figure 34:** The force vs. displacement curves for fine and coarse meshes.

## 5. Conclusion and perspectives

The main objective of this article was to introduce a new algorithm of crack insertion in 3D ductile media called CIPFAR. The algorithm uses a combination of the phase field model adapted for ductile fracture and adaptive remeshing tools. First, an adaptive remeshing strategy is used in order to sufficiently refine the mesh where the crack is expected to propagate. Then, an agnostic crack surface identification method is developed in order to find the intersection of the discrete crack surface with the mesh edges. The method has its root in the domain of image processing and particularly in the edge detection. Next, a unique mesh partitioning strategy is developed in order to locally divide an initial element where the crack surface is expected to cross. Two main advantages arise from the proposed partitioning scheme: (i). the uniqueness of the partitioned elements facilitates the algorithm parallelization; (ii). the algorithm is highly efficient because the partitioning scheme has a linear proportionality to the number of intersected elements, making it perfectly scalable. The next step is the nodal duplication in order to simulate the decohesion of the crack lips. In this regard, the coloring algorithm is used in order to locally determine the number of copies and the elements sharing each copy in what we call a non-manifold mesh repair. Once the crack surfaces are opened, the same operations are repeated until the final crack path is obtained.

Three numerical examples are presented in this article. First, a symmetrically double-notched specimen is used in order to simulate the first mode of fracture. The results have shown that the crack is initiated at the two notches simultaneously and propagated toward the center until the specimen complete fracture is reached. Second, a mixed fracture mode is simulated through a non symmetrically double-notched specimen. It has been shown that two cracks initiate at the two notches and propagate in a curved path toward the center of the specimen which can be observed experimentally. Finally, a flat tensile specimen is tested and results are compared with experimental observations. The main aim of this example was to show the crack initiation at the center of the specimen and the propagation of the crack leading to a horizontal final path with some curvature of the crack lips. In the three examples, a parametric study is carried out to see the effect of phase field and crack insertion models parameters, as well as the effect of mesh size on the final crack path as well as the force vs. displacement curves. The three examples show the robustness of the developed strategy to handle damage to fracture transition in a 3D parallel environment.

The current results are very encouraging to be applied to much complex examples of ductile fracture. The future work is mainly based on two main axes: (i). testing the developed algorithm on metal forming applications in which the crack paths are more complex and the damage evolution depends on the state of the stress such as the stress triaxiality, the Lode parameter and the maximum principal stress; (ii). validation of the numerical model with more experimental results.

# Appendices

## A. Weak formulation of the problem

In this section, the weak form of the phase field for ductile fracture and mechanical equations is demonstrated within the framework of mixed velocity/pressure formulation. The strong form of mechanical equations is written as

$$\begin{cases} \rho \frac{\partial \vec{v}}{\partial t} = \vec{\nabla} \cdot \mathbf{s} - \vec{\nabla} p + \rho \vec{g} \text{ (Conservation of linear momentum)} & (27a) \\ \vec{\nabla} \cdot \vec{v} = -\frac{\dot{p}}{\kappa} \text{ (Conservation of mass)} & (27b) \\ \vec{v} = \vec{v}_0 \text{ on } \partial\Omega_v \text{ (Dirichlet boundary condition)} & (27c) \\ \vec{t} = \vec{t}_0 \text{ on } \partial\Omega_t \text{ (Neumann boundary condition)} & (27d) \end{cases}$$

$$\partial\Omega_h = \partial\Omega_v \cup \partial\Omega_t$$

where  $\mathbf{s}$  is the deviatoric part of the Cauchy stress tensor,  $p$  is the pressure,  $\vec{v}$  is the velocity vector,  $\kappa$  is the bulk's modulus,  $\rho$  is the material density and  $\vec{g}$  is the body force vector per unit mass. The boundary conditions are illustrated in Fig. 2.  $\Omega_h$  is the solid domain in the current configuration,  $\partial\Omega_v$  and  $\partial\Omega_t$  are the predefined boundaries for Dirichlet and Neumann boundary conditions, respectively. The finite element method is used to solve the system of equations 4a and 27. Following the standard Galerkin formulation by multiplying the strong form of partial differential equations by the appropriate test functions leads to the weak form of the following problem:

Find  $(\vec{v}_h, p_h \text{ and } d_h) \in \mathcal{V}_h \otimes \mathcal{P}_h \otimes \mathcal{D}_h$

$$\left\{ \int_{\Omega_h} \left( \rho \frac{\partial \vec{v}_h}{\partial t} \cdot \vec{v}_h^* + \mathbf{s}(\vec{v}_h) : \dot{\boldsymbol{\epsilon}}(\vec{v}_h^*) - p_h \vec{\nabla} \cdot \vec{v}_h^* - \rho \vec{g} \cdot \vec{v}_h^* \right) d\Omega_h = \int_{\partial\Omega_{\vec{t}}} \vec{t}_0 \cdot \vec{v}_h^* d\partial\Omega_h \right. \quad (28a)$$

$$\left. \int_{\Omega_h} p_h^* \vec{\nabla} \cdot \vec{v}_h + \frac{p_h^* \dot{p}_h}{\kappa} d\Omega_h = 0 \right. \quad (28b)$$

$$\left. \int_{\Omega_h} \frac{G_c}{l_c} d_h^* d_h + \int_{\Omega_h} G_c l_c \nabla d_h^* \cdot \nabla d_h d\Omega_h - \int_{\Omega_h} d_h^* \mathcal{H} d\Omega_h = 0 \right. \quad (28c)$$

$$\left. \forall \vec{v}_h^*, p_h^*, d_h^* \in \mathcal{V}_h^0 \otimes \mathcal{P}_h^0 \otimes \mathcal{D}_h^0 \right. \quad (28d)$$

$$\mathcal{V}_h = \left\{ \vec{v}_h \in (H^1)^{\dim(\Omega_h)}, \vec{v}_h = \vec{v}_0 \text{ on } \partial\Omega_e, \forall e \in N_e \right\}$$

$$\mathcal{P}_h = \left\{ p_h \in (C^0)^{\dim(\Omega_e)} \cap L^2, p_h \in P^1 \text{ in } \Omega_e, p_h = p_0 \text{ on } \partial\Omega_e, \forall e \in N_e \right\}$$

$$\mathcal{D}_h = \left\{ d_h^* \in (C^0)^{\dim(\Omega_h)} \cap H^1, d_h \in P^1 \text{ in } \Omega_e, d_h = d_0 \text{ on } \partial\Omega_e, \forall e \in N_e \right\}$$

$$\mathcal{V}_h^0 = \left\{ \vec{v}_h^* \in \mathcal{V}_h, \vec{v}_h = 0 \text{ on } \partial\Omega_e, \forall e \in N_e \right\}$$

$$\mathcal{P}_h^0 = \left\{ p_h^* \in \mathcal{P}_h, p_h = 0 \text{ on } \partial\Omega_e, \forall e \in N_e \right\}$$

$$\mathcal{D}_h^0 = \left\{ d_h^* \in \mathcal{D}_h, d_h = 0 \text{ on } \partial\Omega_e, \forall e \in N_e \right\}$$

the test functions are chosen to be the variations of the unknown variables so that the kinematic admissibility conditions are satisfied at the boundaries.  $\Omega_h$  is the volume of a finite element mesh at the current configuration so that

$$\Omega_h = \bigcup_e \Omega_e (e \in N_e)$$

where  $N_e$  is the number of elements in the mesh.

### A.1. Finite element model

In order to ensure the well-posedness and stability of the numerical solution, a bubble function is introduced to enrich the velocity field. The bubble function should have a value of 1 at the center of the element and vanishes at the boundaries, the resulting velocity and pressure fields of an element in the mesh can be expressed as

$$\vec{v}_h = \vec{v}_l + \vec{v}_b = \sum_{k=1}^{N_n} N_l^k \vec{v}_l^k + \sum_{j=1}^{N_e} N_b^j \vec{v}_b^j \quad (29a)$$

$$p_h = \sum_{k=1}^{N_n} N_l^k P^k \quad (29b)$$

$$d_h = \sum_{k=1}^{N_n} N_l^k d^k \quad (29c)$$

where  $N_l^k$  and  $N_b^k$  are the base and bubble interpolation functions associated with node  $k$ , respectively.  $N_e$  and  $N_n$  are the number of elements and nodes respectively. The resulting system of equations can be written as

$$\left\{ \int_{\Omega_h} \rho \frac{\partial \vec{v}_l}{\partial t} \cdot \vec{v}_l^* + \mathbf{s}(\vec{v}_l) : \dot{\boldsymbol{\epsilon}}(\vec{v}_l^*) - p_h \vec{\nabla} \cdot \vec{v}_l^* - \rho \vec{g} \cdot \vec{v}_l^* d\Omega_h = \int_{\partial\Omega_{\vec{t}}} \vec{t}_0 \cdot \vec{v}_l^* d\Omega_h \quad (30a) \right.$$

$$\left. \int_{\Omega_h} \rho \frac{\partial \vec{v}_b}{\partial t} \cdot \vec{v}_b^* + \mathbf{s}(\vec{v}_b) : \dot{\boldsymbol{\epsilon}}(\vec{v}_b^*) - p_h \vec{\nabla} \cdot \vec{v}_b^* d\Omega_h = \int_{\Omega_h} \rho \vec{g} \cdot \vec{v}_b^* d\Omega_h \quad (30b) \right.$$

$$\left. \int_{\Omega_h} p_h^* \vec{\nabla} \cdot (\vec{v}_l + \vec{v}_b) + \frac{p_h^* \dot{p}_h}{\kappa} d\Omega_h = 0 \quad (30c) \right.$$

$$\left. \int_{\Omega_h} \frac{G_c}{l_c} d_h^* d_h d\Omega_h + \int_{\Omega_h} G_c l_c \frac{\partial d_h}{\partial \vec{x}} \cdot \frac{\partial d_h^*}{\partial \vec{x}} d\Omega_h + \int_{\Omega_h} d_h^* g'(d_h) \mathcal{H} d\Omega_h = 0 \quad (30d) \right.$$

$$\left. \forall (\vec{v}_l^*, \vec{v}_b^*, p_h^*, d_h^*) \in \mathcal{L}_l^0 \otimes \mathcal{L}_b^0 \otimes \mathcal{P}_h^0 \otimes \mathcal{D}_h^0 \quad (30e) \right.$$

$$\mathcal{L}_l^0 = \left\{ \vec{v}_l^* \in (\mathcal{C}^0)^{\dim(\Omega_e)} \cap \mathcal{V}_l^0, \vec{v}_l^* \in P^1 \text{ in } \Omega_e, \vec{v}_l^* = 0 \text{ on } \partial\Omega_e, \forall e \in N_e \right\}$$

$$\mathcal{L}_b^0 = \left\{ \vec{v}_b^* \in (\mathcal{C}^0)^{\dim(\Omega_h)}, \vec{v}_b^* \in P^1 \text{ in } \Omega_e, \vec{v}_b^* = 0 \text{ on } \partial\Omega_e, \forall e \in N_e \right\}$$

with the following properties taken into account:  $\int_{\partial\omega_{\vec{t}}} \vec{t}_0 \cdot \vec{v}_b^* d\omega_h = 0$  since the bubble function vanishes at the boundaries, the inertial contribution of the bubble part is neglected so that  $\int_{\omega_h} \rho \frac{\partial \vec{v}_l}{\partial t} \cdot \vec{v}_b^* d\Omega_h = \int_{\omega_h} \rho \frac{\partial \vec{v}_b}{\partial t} \cdot \vec{v}_l^* d\Omega_h = 0$  and  $\int_{\Omega_h} \mathbf{s}(\vec{v}_b) : \dot{\boldsymbol{\epsilon}}(\vec{v}_l^*) d\omega_h = \int_{\omega_h} \mathbf{s}(\vec{v}_l) : \dot{\boldsymbol{\epsilon}}(\vec{v}_b^*) d\Omega_h = 0$  due to the orthogonality property of the bubble and nodal spaces. The time derivative of the velocity is approximated as follows

$$\frac{\partial \vec{v}_{l,b}}{\partial t} = \frac{\vec{v}_{l,b}^{t+\Delta t} - \vec{v}_{l,b}^t}{\Delta t}$$

where  $\Delta t$  is the time step. Substituting equations 29 and A.1 in A.2, the final form of the residual equations can be written on the following form:

$$\mathbf{R}^{ll} + \mathbf{R}^{lp} = \mathbf{0} \quad (31a)$$

$$\mathbf{R}^{bb} + \mathbf{R}^{bp} = \mathbf{0} \quad (31b)$$

$$\mathbf{R}^{pl} + \mathbf{R}^{pb} + \mathbf{R}^{pp} = \mathbf{0} \quad (31c)$$

$$\mathbf{R}^{dd} + \mathbf{R}^{dl} = \mathbf{0} \quad (31d)$$

where  $\mathbf{R}^{xy}$  is the residual force vector of coupled set of unknowns  $x$  and  $y$ . The system of equations in 31 will be solved in a staggered manner. A Newton Raphson nonlinear solver is used to solve the system of the first three equations before each remeshing step. Then, the fourth equation will be solved independently. It is worth noting that the system of equations 31a, 31b and 31c are condensed so that the final unknowns become the velocities and pressures at the nodes without the need to explicitly solve for the bubble velocities.

## Acknowledgements

This research was funded by the enterprise of Transvalor with mutual cooperation with the center of material forming (CEMEF)

## References

- [1] A. A. Griffith, The phenomena of rupture and flow in solids, Philosophical transactions of the royal society of london. Series A, containing papers of a mathematical or physical character 221 (1921) 163–198.
- [2] G. R. Irwin, Analysis of stresses and strains near the end of a crack transversing a plate, Trans. ASME, Ser. E, J. Appl. Mech. 24 (1957) 361–364.
- [3] G. A. Francfort, J.-J. Marigo, Revisiting brittle fracture as an energy minimization problem, Journal of the Mechanics and Physics of Solids 46 (1998) 1319–1342.
- [4] L. Ambrosio, V. M. Tortorelli, Approximation of functional depending on jumps by elliptic functional via t-convergence, Communications on Pure and Applied Mathematics 43 (1990) 999–1036.
- [5] M. Ambati, T. Gerasimov, L. De Lorenzis, Phase-field modeling of ductile fracture, Computational Mechanics 55 (2015) 1017–1040.
- [6] M. Ambati, R. Kruse, L. De Lorenzis, A phase-field model for ductile fracture at finite strains and its experimental verification, Computational Mechanics 57 (2016) 149–167.
- [7] M. J. Borden, T. J. R. Hughes, C. M. Landis, A. Anvari, I. J. Lee, A phase-field formulation for fracture in ductile materials: Finite deformation balance law derivation, plastic degradation, and stress triaxiality effects, Computer Methods in Applied Mechanics and Engineering 312 (2016) 130–166.
- [8] J. Besson, Continuum models of ductile fracture: a review, International Journal of Damage Mechanics 19 (2010) 3–52.

- [9] J. Mediavilla, M. G. D. Peerlings, R.H.J. as, Discrete crack modelling of ductile fracture driven by non-local softening plasticity, *International journal for numerical methods in engineering* 66 (2006) 661–688.
- [10] A. L. Gurson, Continuum theory of ductile rupture by void nucleation and growth: Part 1—yield criteria and flow rules for porous ductile media, *Journal of Engineering Materials and Technology* 99 (1977) 2–15.
- [11] V. Tvergaard, A. Needleman, Analysis of the cup-cone fracture in a round tensile bar, *Acta metallurgica* 32 (1984) 157–169.
- [12] J. Lemaitre, A continuous damage mechanics model for ductile fracture, *Journal of engineering materials and technology* 107 (1985) 83–89.
- [13] P.-O. Bouchard, L. Bourgeon, S. Fayolle, K. Mocellin, An enhanced lemaître model formulation for materials processing damage computation, *International Journal of Material Forming* 4 (2011) 299–315.
- [14] T.-S. Cao, J.-M. Gachet, P. Montmitonnet, P.-O. Bouchard, A lode-dependent enhanced lemaître model for ductile fracture prediction at low stress triaxiality, *Engineering Fracture Mechanics* 124 (2014) 80–96.
- [15] S. Feld-Payet, V. Chiaruttini, J. Besson, F. Feyel, A new marching ridges algorithm for crack path tracking in regularized media, *International Journal of Solids and Structures* 71 (2015) 57–69.
- [16] J.-P. Thirion, A. Gourdon, The marching lines algorithm: new results and proofs (1993).
- [17] T. Belytschko, T. Black, Elastic crack growth in finite elements with minimal remeshing, *International journal for numerical methods in engineering* 45 (1999) 601–620.
- [18] M. R. Seabra, J. M. C. de Sa, P. Šuštarčič, T. Rodič, Some numerical issues on the use of xfem for ductile fracture, *Computational mechanics* 50 (2012) 611–629.
- [19] P.-O. Bouchard, F. Bay, Y. Chastel, Numerical modelling of crack propagation: automatic remeshing and comparison of different criteria, *Computer methods in applied mechanics and engineering* 192 (2003) 3887–3908.
- [20] A. Hussein, B. Hudobivnik, P. Wriggers, A combined adaptive phase field and discrete cutting method for the prediction of crack paths, *Computer Methods in Applied Mechanics and Engineering* 372 (2020) 113329.
- [21] F. Aldakheel, B. Hudobivnik, P. Wriggers, Virtual element formulation for phase-field modeling of ductile fracture, *International Journal for Multiscale Computational Engineering* 17 (2019).
- [22] A. Hussein, B. Hudobivnik, F. Aldakheel, P. Wriggers, P.-A. Guidault, O. Allix, A virtual element method for crack propagation, *PAMM* 18 (2018) e201800104.
- [23] D. Uribe-Suárez, P.-O. Bouchard, M. Delbo, D. Pino-Muñoz, Numerical modeling of crack propagation with dynamic insertion of cohesive elements, *Engineering Fracture Mechanics* 227 (2020) 106918.

- [24] D. Mumford, J. Shah, Optimal approximations by piecewise smooth functions and associated variational problems, *Communications on pure and applied mathematics* 42 (1989) 577–685.
- [25] C. Miehe, M. Hofacker, F. Welschinger, A phase field model for rate-independent crack propagation: Robust algorithmic implementation based on operator splits, *Computer Methods in Applied Mechanics and Engineering* 199 (2010) 2765–2778.
- [26] I. Babuška, The finite element method with lagrangian multipliers, *Numerische Mathematik* 20 (1973) 179–192.
- [27] R. Pierre, Optimal selection of the bubble function in the stabilization of the p1-p1 element for the stokes problem, *SIAM journal on numerical analysis* 32 (1995) 1210–1224.
- [28] H. Eldahshan, P.-O. Bouchard, J. Alves, E. Perchat, D. P. Munoz, Phase field modeling of ductile fracture at large plastic strains using adaptive isotropic remeshing, *Computational Mechanics* 67 (2021) 763–783.
- [29] D. W. Matula, G. Marble, J. D. Isaacson, Graph coloring algorithms, in: *Graph theory and computing*, Elsevier, 1972, pp. 109–122.
- [30] M. Shakoor, M. Bernacki, P.-O. Bouchard, A new body-fitted immersed volume method for the modeling of ductile fracture at the microscale: Analysis of void clusters and stress state effects on coalescence, *Engineering Fracture Mechanics* 147 (2015) 398–417.
- [31] D. Eberly, R. Gardner, B. Morse, S. Pizer, C. Scharlach, Ridges for image analysis, *Journal of Mathematical Imaging and Vision* 4 (1994) 353–373.
- [32] S. Kumar, L. Fourment, S. Guerdoux, Parallel, second-order and consistent remeshing transfer operators for evolving meshes with superconvergence property on surface and volume, *Finite Elements in Analysis and Design* 93 (2015) 70–84.
- [33] O. C. Zienkiewicz, J. Zhu, The superconvergent patch recovery (spr) and adaptive finite element refinement, *Computer Methods in Applied Mechanics and Engineering* 101 (1992) 207–224.
- [34] T. Coupez, S. Marie, R. Ducloux, Parallel 3d simulation of forming processes including parallel remeshing and reloading, in: *Numerical Methods in Engineering’96 (Proceedings of 2nd ECCOMAS Conference, J.-A. Désidéri et. al. Editors)*, 1996, pp. 738–743.
- [35] M. J. Borden, C. V. Verhoosel, M. A. Scott, T. J. R. Hughes, C. M. Landis, A phase-field description of dynamic brittle fracture, *Computer Methods in Applied Mechanics and Engineering* 217 (2012) 77–95.
- [36] A. Ghahremaninezhad, K. Ravi-Chandar, Ductile failure behavior of polycrystalline al 6061-t6, *International journal of fracture* 174 (2012) 177–202.